Obesity-dependent changes in interstitial ECM mechanics promote breast tumorigenesis

Bo Ri Seo,[1] Priya Bhardwaj,[2] Siyoung Choi,[1] Jacqueline Gonzalez,[1] Roberto C. Andresen Eguiluz,[3] Karin Wang,[1,3] Sunish Mohanan,[4] Patrick G. Morris,[5] Baoheng Du,[2] Xi K. Zhou,[6] Linda T. Vahdat,[2] Akanksha Verma,[7] Olivier Elemento,[7] Clifford A. Hudis,[5] Rebecca M. Williams,[1] Delphine Gourdon,[3] Andrew J. Dannenberg,[2] Claudia Fischbach[1,8]*

Obesity and extracellular matrix (ECM) density are considered independent risk and prognostic factors for breast cancer. Whether they are functionally linked is uncertain. We investigated the hypothesis that obesity enhances local myofibroblast content in mammary adipose tissue and that these stromal changes increase malignant potential by enhancing interstitial ECM stiffness. Indeed, mammary fat of both diet- and genetically induced mouse models of obesity were enriched for myofibroblasts and stiffness-promoting ECM components. These differences were related to varied adipose stromal cell (ASC) characteristics because ASCs isolated from obese mice contained more myofibro- blasts and deposited denser and stiffer ECMs relative to ASCs from lean control mice. Accordingly, decellularized matrices from obese ASCs stimulated mechanosignaling and thereby the malignant potential of breast cancer cells. Finally, the clinical relevance and translational potential of our findings were supported by analysis of patient speci- mens and the observation that caloric restriction in a mouse model reduces myofibroblast content in mammary fat. Collectively, these findings suggest that obesity-induced interstitial fibrosis promotes breast tumorigenesis by altering mammary ECM mechanics with important potential implications for anticancer therapies.

INTRODUCTION

Obesity, with increasing worldwide prevalence, is a key risk factor for the development and prognosis of breast cancer (*1*). This correlation has been commonly attributed to obesity-mediated differences in adipose endocrine functions (*2*). However, given the critical role of contextual cues in tumorigenesis, obesity-mediated alterations to the local microenvironment may also be important. In particular, obesity induces fibrotic remodeling of adipose tissue (*3*), and these changes have been associated with malignant potential (*4*). Nevertheless, the exact mechanisms through which interstitial fibrosis in obese adipose tissue may affect the pathogenesis of breast cancer remain largely elusive.

Similar to obesity, tumors also feature fibrosis in the surrounding stroma, which is commonly referred to as desmoplasia. The concomitant changes in extracellular matrix (ECM) density and rigidity not only enable detection by mammography and palpation, respectively, but also represent important risk factors for tumor development, progression, and response to therapy (*5*, *6*). More specifically, enhanced stiffness changes cellular mechanosignaling (*7*), which, in turn, stimulates more aggressive behavior in cancer cells through various mechanisms including perturbed epithelial morphogenesis (*8*), growth factor and cytokine signaling (*9*), and stem cell differentiation (*10*, *11*). However, whether obesity-associated fibrotic remodeling alters local ECM mechanical properties and whether these differences activate protumorigenic mechanotransduction remain to be elucidated.

[1]Department of Biomedical Engineering, Cornell University, Ithaca, NY 14853, USA. [2]Department of Medicine, Weill Cornell Medical College, New York, NY 10065, USA. [3]Department of Materials Science and Engineering, Cornell University, Ithaca, NY 14853, USA. [4]Department of Biological and Biomedical Sciences, Cornell University, Ithaca, NY 14853, USA. [5]Department of Medicine, Memorial Sloan Kettering Cancer Center, New York, NY 10065, USA. [6]Department of Healthcare Policy and Research, Weill Cornell Medical College, New York, NY 10065, USA. [7]Department of Physiology and Biophysics, Institute for Computational Biomedicine, Weill Cornell Medical College, New York, NY 10065, USA. [8]Kavli Institute at Cornell for Nanoscale Science, Cornell University, Ithaca, NY 14853, USA.
*Corresponding author. E-mail: cf99@cornell.edu

Myofibroblasts are major cellular regulators of fibrotic and desmoplastic remodeling and, thus, tissue mechanical properties (*12*). Myofibroblasts are highly contractile and assemble a fibronectin- and collagen type I–rich ECM that is characterized by enhanced density, fibrillar architecture, cross-linking, and partial unfolding—all parameters causally linked to increased ECM stiffness (*11*–*13*). Various proinflammatory cytokines enhanced during obesity [for example, transforming growth factor–b1 (TGF-b1) (*14*)] can initiate myofibroblast differentiation in mesenchymal cells, including adipose stem cells (ASCs) (*11*). Nevertheless, the impact of obesity on myofibroblast content of mammary adipose tissue remains uncertain as most previous studies were performed with subcutaneous and visceral fat. Extrapolation of such results to mammary fat should be avoided because both global functions (*15*) and fibrotic remodeling (*16*) of adipose tissue can vary significantly between anatomic depots.

Here, our goal was to characterize the role of obesity in interstitial fibrosis in mammary fat, determine the impact of these variations on ECM mechanical properties, and assess whether these changes enhance myofibroblast content and the malignant potential of mammary tumor cells due to altered mechanotransduction. We have applied a multidisciplinary approach that integrates biological and physical techniques to mouse and human samples, ultimately extending our quantitative understanding of the functional relationship between obesity-induced alterations in ECM mechanics as it pertains to enhanced breast carcinogenesis. Consequently, the risk and prognosis of breast cancer patients may be more accurately predicted, and therapeutic interference with the suggested relationship may improve patients' outcomes.

RESULTS

Obesity increases interstitial fibrosis in mouse mammary fat pads To quantify fibrotic remodeling, we assessed myofibroblast content and related ECM changes in mammary adipose tissue harvested from two

established mouse models of obesity. Diet-induced obesity was achieved by feeding a high-fat diet to female C57BL/6J mice for 10 weeks starting at 5 weeks of age (Fig. 1A). Obesity was reflected by increased weight of these mice relative to lean control animals fed a low-fat diet (29.7 ± 4.2 g versus 21.2 ± 0.6 g; mean ± SD, $n = 20$ per group). Additionally, we used female *ob/ob* mice, which are morbidly obese compared to age-matched wild-type mice (54.4 ± 2.9 g versus 19.8 ± 1.5 g; mean ± SD, $n = 10$ per group) (Fig. 1A) owing to a loss-of-function mutation in the gene encoding the satiety hormone leptin (*17*). Histological evaluation of hematoxylin and eosin (H&E)–stained sections showed global differences of obese versus lean breast adipose tissue, including larger adipocytes (Fig. 1B). Additionally, immunofluorescence analysis suggested that both diet- and genetically induced obesity enhanced levels of interstitial a–smooth muscle actin (a-SMA), a myofibroblast marker, relative to the respective controls (Fig. 1C). This was further confirmed by Western blot analysis of mammary adipose tissue from diet-induced mouse models. The levels of fibronectin, an ECM component primarily deposited by myofibroblasts (*12*), were also enhanced in obese animals (Fig. 1D).

High-fat diet increased a-SMA and fibronectin content in the mammary adipose tissue of both ovary-intact mice and ovariectomized mice (fig. S1, A to C). These data suggest that the profibrotic changes after menopause are relevant to postmenopausal breast cancer, which is where the link between obesity and risk of breast cancer is clearest (*18*). Ovariectomy did not further stimulate a-SMA in response to high-fat diet relative to intact animals ($P = 0.97$, Student's t test), although ovariectomy with high-fat diet increased mouse weight compared with high-fat diet alone [24.4 ± 2.8 g (ovariectomy/low-fat diet); 38.9 ± 2.9 g (ovariectomy/high-fat diet); 29.74 ± 4.15 g (high-fat diet); mean ± SD, $n = 20$ per group]. Although this increase in weight is accompanied by elevated mammary gland inflammation (*19*), our results imply that inflammation may not be the sole regulator of obesity-induced fibrosis.

In addition to fibrosis, tissues were analyzed for the effect of obesity on ECM structure. Second harmonic generation (SHG) imaging was

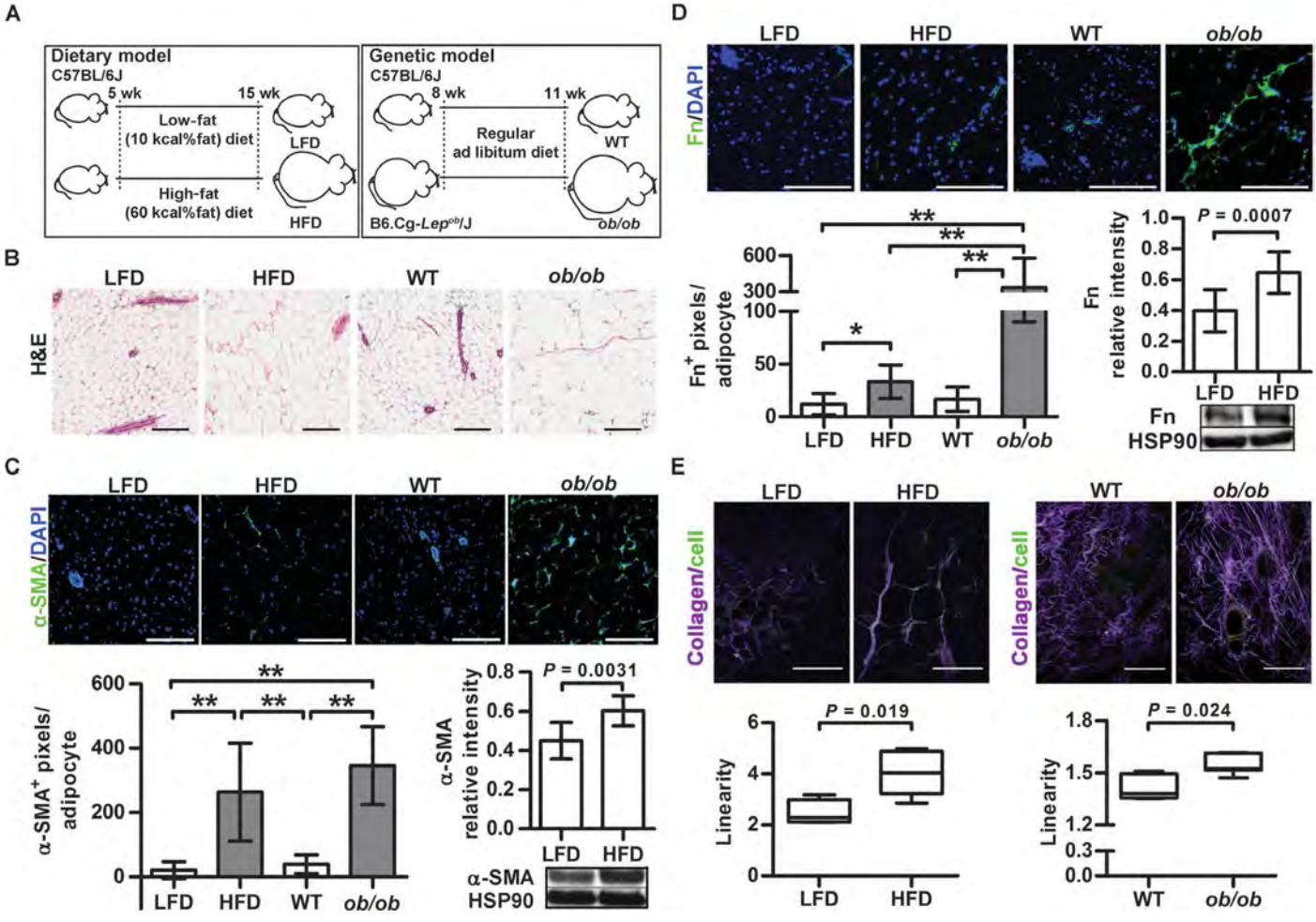

Fig. 1. Obesity increases interstitial fibrosis in mouse mammary fat pads. (A) Schematic showing the dietary [high-fat diet (HFD) and low-fat diet (LFD), 15 weeks] and genetic [*ob/ob* and wild-type (WT), 11 weeks] mouse models of obesity that were used to compare fibrotic remodeling between lean and obese mammary fat. (B) H&E-stained sections of mammary fat from lean and obese mice. Scale bars, 200 mm. (C and D) Immunofluorescence and Western blot analysis of a-SMA (C) and fibronectin (Fn) (D) in mammary fat. Scale bars, 200 mm. Western blot quantification is relative to the corresponding HSP90 levels. (E) SHG imaging of collagen fiber linearity in mammary fat. Box plots show medians with whiskers from minimum to maximum values. Scale bars, 100 mm. (C to E) Data are means ± SD ($n = 6$ to 11 per group). *$P < 0.05$, **$P < 0.01$, unless otherwise noted, by unpaired Student's two-tailed t tests for two conditions and one-way analysis of variance (ANOVA) for multiple comparisons. DAPI, 4′,6-diamidino-2-phenylindole.

used to quantify ECM structural changes. Interstitial collagen was more linearized in mammary adipose tissue of obese animals in both diet- and genetically induced obesity models (Fig. 1E). Thus, obesity caused structural changes of collagen that have been previously associated with ASC-mediated ECM remodeling, enhanced stiffness, and tumor malignancy in mice and humans (*11*, *13*, *20*). In summary, obesity initiates fibrotic remodeling of mammary adipose tissue by triggering molecular, cellular, and ECM structural changes.

Obesity enhances the profibrotic phenotype of ASCs

To investigate cellular and molecular differences in obese and lean animals, we compared both the myofibroblast content and the ECM remodeling capacity of ASCs isolated from adipose tissue (Fig. 2A). Only a small quantity of ASCs can be isolated from mammary adipose tissue, and differences in mammary fat were comparable to those present in inguinal (a mix of subcutaneous and mammary) depots (fig. S2, A to C); thus, ASCs were isolated from the stromal vascular fraction of inguinal adipose tissue from age-matched wild-type and *ob/ob* mice (20.2 ± 1.4 g versus 56.6 ± 3.3 g; mean ± SD). Indeed, ASCs from obese mice were enriched for a-SMA$^+$ myofibroblasts (Fig. 2B). Furthermore, these cells also exhibited enhanced proliferative capacity (Fig. 2C) and secreted more stromal cell–derived factor 1 (SDF-1) (Fig. 2D)—both markers of myofibroblasts or activated fibroblasts (*21*, *22*)—than their lean counterparts. Finally, as compared to wild-type ASCs, *ob/ob* ASCs assembled thicker ECMs enriched with collagen and fibronectin (Fig. 2, E and F), further confirming the profibrotic phenotype of these cells.

Next, we verified that the above-described cellular changes were universal rather than limited to the genetic makeup of *ob/ob* ASCs. We performed experiments with ASCs isolated from the diet-induced mouse model of obesity as well as *ob/ob* ASCs supplemented with leptin to

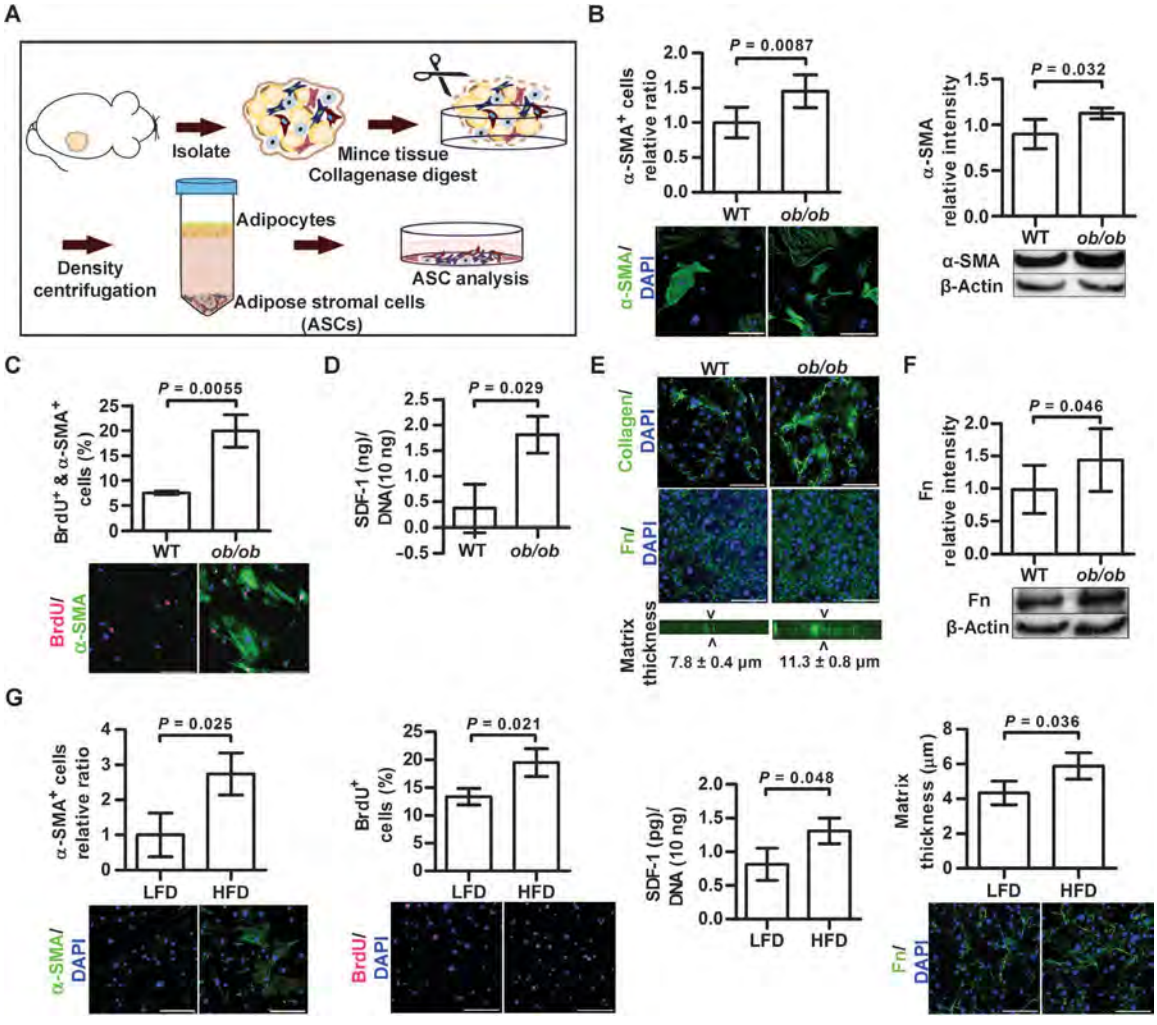

Fig. 2. Obesity enhances the profibrotic phenotype of ASCs. (A) Schematic showing ASC isolation from inguinal fat of age-matched lean and obese mice. (B) Immunofluorescence analysis of a-SMA$^+$ ASCs isolated from *ob/ob* relative to WT fat. Western blot analysis of a-SMA relative to b-actin. (C) Percentage of a-SMA$^+$ and BrdU$^+$ ASCs as analyzed by immunofluorescence. (D) SDF-1 secretion of WT and *ob/ob* ASCs as determined by enzyme-linked immunosorbent assay (ELISA) and normalized to DNA content. (E) Confocal analysis of collagen type I or fibronectin deposition by WT and *ob/ob* ASCs. (F) Western blot quantification of fibronectin deposition relative to b-actin. (G) Comparison of ASCs isolated from low-fat diet– and high-fat diet–fed mice for a-SMA levels and BrdU incorporation by immunofluorescence; SDF-1 secretion by ELISA; and fibronectin matrix deposition by confocal microscopy. Scale bars, 200 mm. (B to G) Data are means ± SD (n = 3 to 6 per condition). P values by unpaired two-tailed t tests.

reconstitute the leptin-mediated effects on cellular phenotype that are independent from satiety regulation. ASCs isolated from inguinal fat of mice fed a high-fat diet had elevated a-SMA levels, proliferative capacity, SDF-1 secretion, and matrix deposition, similar to ASCs from *ob/ob* mice (Fig. 2G). Leptin supplementation did not mitigate the increased profibrotic potential of *ob/ob* ASCs because neither a-SMA levels nor fibronectin deposition significantly decreased with this treatment (fig. S3, A and B).

Collectively, these results suggest that obesity promotes ECM remodeling by increasing the myofibroblast content of the adipose stromal vascular fraction in both diet- and genetically induced mouse models of obesity, regardless of ovary function. Thus, we performed all following experiments with *ob/ob* ASCs.

Obesity-associated ASCs deposit partially unfolded and stiff ECMs

Given that myofibroblast-mediated changes of ECM composition and structure can increase malignancy by changing microenvironmental stiffness, we next tested whether the obesity-mediated effects on ASCs translate to altered ECM mechanics. Although increased rigidity of fibrotic and tumor tissue is typically believed to reflect alterations in collagen synthesis and cross-linking (*13*), variations in the fibronectin matrix structure and mechanics may be equally important. In fact, cellular deposition and remodeling of fibronectin is critical to the formation and turnover of collagen I–based ECMs (*23*), and both fibronectin conformational and mechanical changes may play an important role in this process (*24*, *25*). Förster resonance energy transfer (FRET) analysis of fibronectin conformation indicated that ASCs isolated from obese mice partially unfold fibronectin matrix fibers (Fig. 3, A and B) thereby mimicking fibronectin changes mediated by tumor-associated ASCs (*26*).

Partial fibronectin unfolding may change cellular behavior not only by exposing cryptic sites (*27*) or disrupting strain-sensitive binding sites, such as the a_5b_1 integrin binding site (*28*), but also by directly elevating fibronectin fiber rigidity (*26*). To confirm that obesity affects the rigidity of ASC-deposited ECMs at the cellular/matrix level, we performed quasistatic compressive measurements with the surface forces apparatus (SFA) (Fig. 3C) (*27*). Our results verified that obesity elevates matrix rigidity (Fig. 3D), a phenomenon associated with malignancy (*8*). The determined elastic moduli were relatively low compared with previously reported tumor stiffness (*8*), given our specific sample preparation technique (measurements of decellularized, nonfixed ECMs immersed in saline). Nevertheless, they are relevant because the stiffness of ECMs deposited by tumor-conditioned ASCs under the same experimental conditions was in a similar compliant range and was increased relative to control ASCs (*27*). Lastly, analysis of interstitial mechanics of breast tissue from wild-type and *ob/ob* mice with atomic force microscopy (AFM) nanoindentation further validated that the

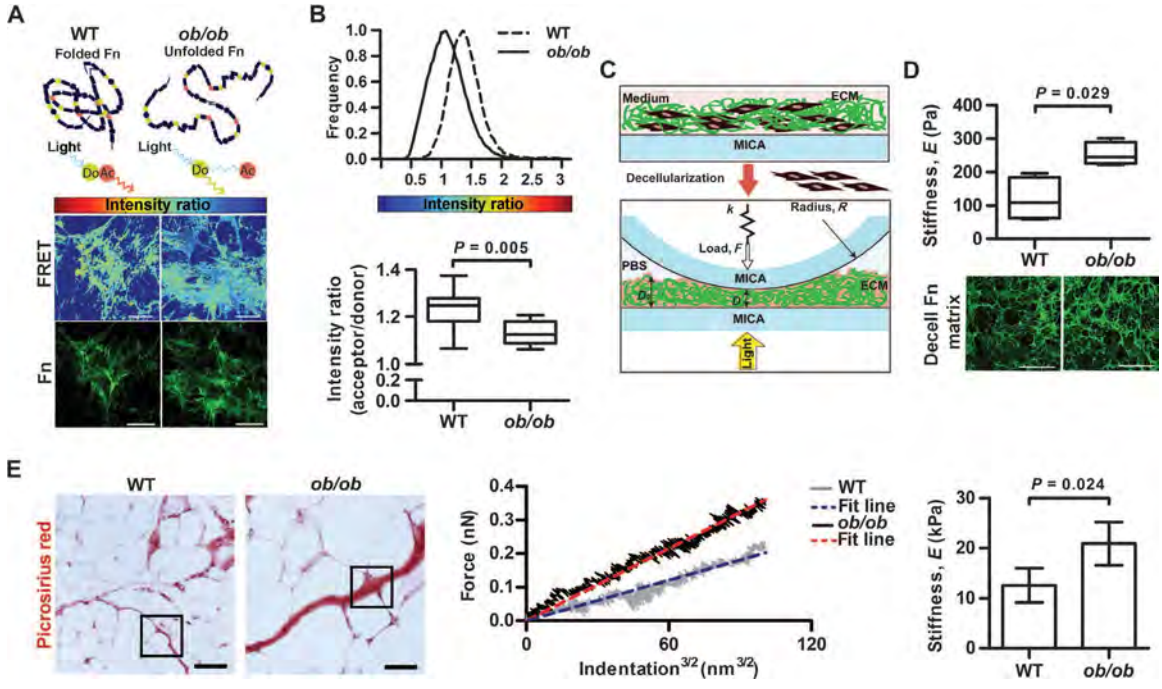

Fig. 3. Obesity-associated ASCs deposit partially unfolded and stiffer ECMs. (A) FRET analysis of fibronectin conformation in ECMs deposited by WT or *ob/ob* ASCs. Schematic shows separation of donor (Do) and acceptor (Ac) fluorophores due to partial fibronectin unfolding. Pseudocolored immunofluorescence micrographs depict FRET intensities of fibronectin fibers in the different ECMs. Scale bars, 50 mm. (B) Representative histogram of FRET intensity distribution as analyzed from the fields of view shown in (A). Box and whisker plots of FRET intensities as analyzed from six to eight representative fields of view per condition. Data are medians with whiskers from minimum to maximum values. (C) SFA indentation analysis of decellularized ECMs between two silvered mica surfaces mounted on a cantilever spring of constant *k*. *F* is normal force; *R* is the radius of curvature of the cylindrical discs; D_0 and *D* are the undistorted and force-applied thicknesses of the matrix, respectively. (D) Compressive elastic moduli of decellularized ECMs with corresponding fibronectin immunofluorescence micrographs. Box plots show medians with whiskers from minimum to maximum values from four random fields per condition. Scale bars, 100 mm. (E) AFM analysis to assess the elastic moduli of interstitial mammary fat. (Left) Picrosirius Red–stained histological cross sections showing representative regions of analysis. (Middle) Representative force versus indentation curve. (Right) Data are average compressive elastic moduli ± SD, analyzed from four samples per condition (20 areas per sample). Scale bars, 100 mm. *P* values in (B), (D), and (E) were determined by unpaired two-tailed *t* tests. PBS, phosphate-buffered saline.

stiffness of interstitial adipose tissue increases with obesity (Fig. 3E). Consequently, obesity affects the mechanical properties of the ECM deposited by ASCs, which may ultimately lead to interstitial stiffening.

ASCs isolated from visceral fat of *ob/ob* mice similarly exhibited enhanced profibrotic potential compared with those from the wild-type, as detected by elevated a-SMA and fibronectin content and partial unfolding of deposited fibronectin matrices (fig. S4, A to C). However, in wild-type animals, visceral fat not only contained fewer a-SMA$^+$ASCs than inguinal fat (24.8 ± 2.4% versus 39.2 ± 16.2%; mean ± SD, n = 3 per group), but visceral fat–derived wild-type ASCs also deposited less ECM compared with wild-type ASCs from inguinal fat (fig. S4D). These results suggest that obesity may alter the mechanical properties of adipose interstitial tissue at varying anatomical depots, but that the extent of these changes may be enhanced at inguinal relative to visceral sites.

ECM deposited by obesity-associated ASCs promote myofibroblast differentiation via altered mechanosignaling

We next tested whether the changes in ECM physicochemical properties directly contribute to the increased levels of myofibroblasts in obese adipose tissue (fig. S5A) because it has been shown that elevated ECM stiffness can promote myofibroblast differentiation (*29*). Wild-type ASCs exhibited enhanced a-SMA levels when cultured on decellularized matrices deposited by *ob/ob* ASCs versus wild-type ASCs, whereas the wild-type ECMs did not affect a-SMA protein expression in *ob/ob* ASCs (fig. S5B). The presence of the Rho-associated protein kinase (ROCK) inhibitor Y27632 did not elevate a-SMA in wild-type ASCs cultured in *ob/ob* ECM, indicating that ECM-induced differences were related to varied cell contractility and, thus, mechanotransduction. Inhibition of cell contractility with Y27632 reduced a-SMA in *ob/ob* ASCs on both types of decellularized ECM (fig. S5B), consistent with previous findings that contractility is mandatory for maintenance of the myofibroblast phenotype (*30*).

The amount of endogenously sequestered TGF-b was similar in both types of decellularized ECM (fig. S5C), and saturating TGF-b–binding sites in the different ECMs (by incubation with exogenous TGF-b before cell seeding) had no significant effect on a-SMA protein expression (fig. S5D). Differential mechanical activation of latent, ECM-sequestered TGF-b (*31*) was not responsible for the myofibroblastic cell population because we observed no marked difference in a-SMA levels when latency-associated peptide (LAP), a cellular force transmission molecule, was functionally inhibited (fig. S5D). Collectively, these findings suggest that the varied ECM physicochemical properties of obese interstitial adipose tissue provide a direct, TGF-b–independent positive feedback mechanism that elevates myofibroblast content in obese adipose tissue.

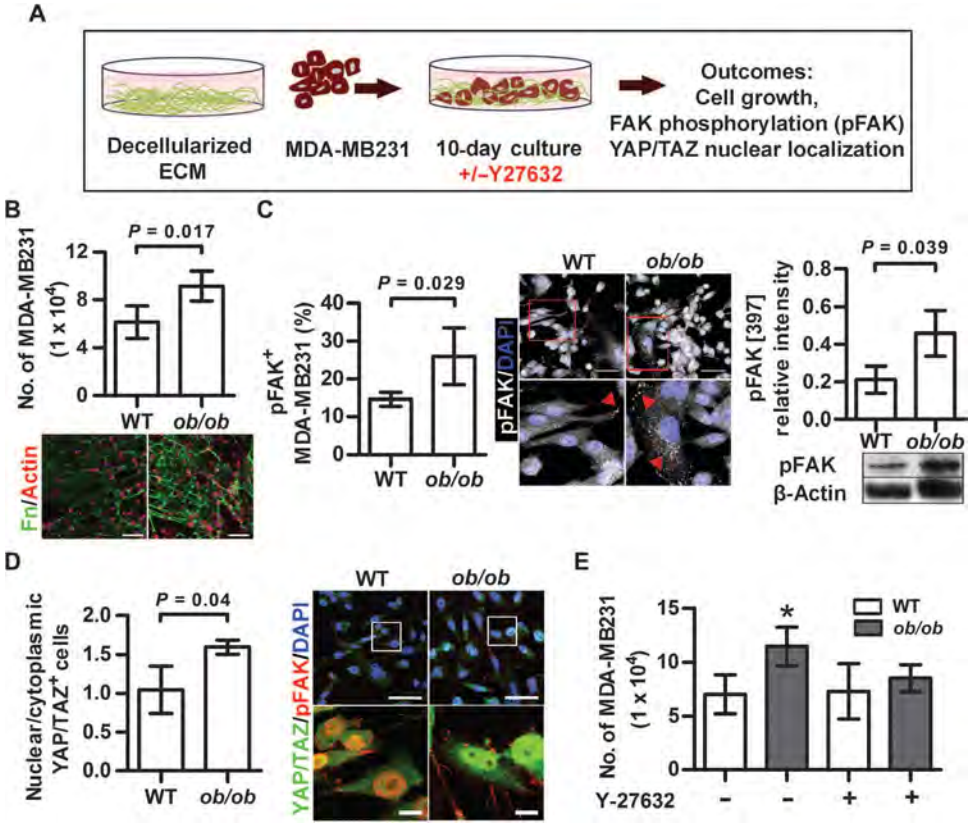

Fig. 4. ECMs deposited by obesity-associated ASCs stimulate MDA-MB231 mechanosensitive growth. (A) Experimental setup to analyze human breast cancer cell line MDA-MB231 behavior in response to decellularized WT and *ob/ob* ECMs. (B) Number of MDA-MB231 cells after culture on decellularized *ob/ob* or WT ECMs as determined by image analysis. Scale bar, 100 mm. (C) Immunofluorescence analysis of pFAK[397]$^+$ MDA-MB231 (red arrows) after culture on the different ECMs and corresponding Western blot analysis of pFAK[397] relative b-actin. Scale bars, 50 mm. (D) Immunofluorescence analysis of the nuclear/cytoplasmic YAP/TAZ ratio of MDA-MB231 after culture on *ob/ob* or WT ECMs. Scale bars, 50 mm (top); 20 mm (bottom). *P* values in (B) to (D) determined by unpaired two-tailed *t* tests. (E) Effect of Y27632 on MDA-MB231 growth on *ob/ob* or WT ECMs as assessed by image analysis of cell number. *P < 0.05 versus all other groups, determined by two-way ANOVA. (B to E) Data are means ± SD (n = 3 per condition).

Obesity-associated ASCs stimulate breast cancer mechanosensitive growth

Next, we examined the impact of obesity-associated ECM remodeling on mammary tumor cells by seeding MDA-MB231 human breast cancer cells onto decellularized matrices assembled by age-matched wild-type and *ob/ob* ASCs (Fig. 4A). In line with the observation that ASC-derived myofibroblasts deposit ECMs that promote breast cancer cell proliferation (*11*), MDA-MB231 growth was significantly enhanced on *ob/ob* ECMs (Fig. 4B). Given that *ob/ob* ASCs can unfold fibronectin, which in turn can alter cell behavior by modulating binding specificity of synergy-dependent (for example, a_5b_1) and non–synergy-dependent (for example, a_vb_3) integrins (*28*, *32*), we first tested whether the detected differences in tumor cell growth were due to fibronectin conformation–dependent variations in a_5b_1 and a_vb_3 engagement. Supplementation of neither a_5b_1 nor a_vb_3 function–blocking antibodies significantly affected MDA-MB231 growth on wild-type or *ob/ob* matrices (fig. S6A). These data indicate that fibronectin conformational changes are not primarily responsible for the differential tumor cell

response, leading us to investigate ECM-induced differences in tumor cell mechanosignaling.

Increased stiffness stimulates tumor cell growth by altering mechanotransduction in a sequence of events, including enhanced RhoA/ROCK-mediated cell contractility, phosphorylation of focal adhesion kinase (pFAK), and ultimately YAP/TAZ transcription factor activity (*33*, *34*). We found that MDA-MB231 cells contained not only more pFAK (Fig. 4C) but also more nuclear YAP/TAZ (Fig. 4D) when seeded onto ECMs deposited by *ob/ob* compared with wild-type ASCs. Moreover, inhibition of cell contractility with the ROCK inhibitor Y27632 blocked the growth-promoting effect of ECMs deposited by *ob/ob* ASCs (Fig. 4E), which was paralleled by a reduction in pFAK (fig. S6B). These data imply that obesity-induced interstitial ECM stiffness promotes tumor cell growth by altering cell contractility–dependent signal transduction.

Obesity-associated differences in local interstitial stiffness are relevant even to tumor cells not directly in contact with these sites, as the increased levels of SDF-1 secreted by obese ASCs (Fig. 2D) stimulated MDA-MB231 migration via the SDF-1/CXCR4 signaling axis as compared to a similar number of lean ASCs (fig. S6C).

Obesity-associated ECMs promote the tumorigenic potential of premalignant human breast epithelial cells

To assess whether the detected differences in obesity-associated ECM remodeling also drive the transformation of premalignant cells, we performed experiments with premalignant MCF10AT human breast epithelial cells (*35*). Indeed, *ob/ob* ASC–derived decellularized ECMs promoted the growth of MCF10AT cells because of matrix-induced changes in cell contractility as confirmed by blockade of Rho/ROCK signaling with Y27632 (Fig. 5A).

Additionally, we tested the effect of the different matrices on the disorganization of three-dimensional (3D) MCF10AT acini, a hallmark of malignant transformation (*8*, *36*). Structurally intact MCF10AT mammary acini were seeded onto either wild-type or *ob/ob* ECMs (Fig. 5B). Acini cultured on *ob/ob* matrices were significantly more disorganized relative to acini cultured on the corresponding wild-type matrices (Fig. 5C). To confirm that these differences were not solely due to changes of cell proliferation, we analyzed MCF10AT cell migration on the different ECMs. The *ob/ob* ECMs promoted the migration of premalignant MCF10AT cells along ECM fibers (Fig. 5D, i) and away from their original position (Fig. 5D, ii) more so than did wild-type ECMs. Additionally, quantification of motility over the course of 5 hours confirmed the increased migration speed of MCF10AT cells on *ob/ob* ECMs (Fig. 5D, iii).

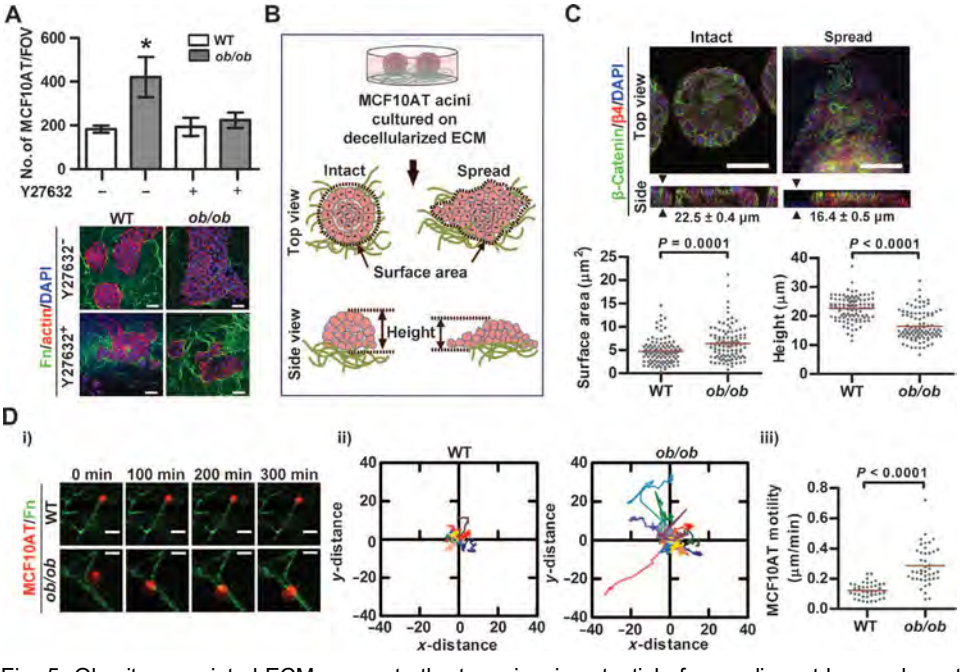

Fig. 5. Obesity-associated ECMs promote the tumorigenic potential of premalignant human breast epithelial cells. (A) Number of MCF10AT cells after culture on WT or *ob/ob* ECMs in the presence and absence of Y27632. Data are means ± SD ($n = 3$). *$P < 0.05$ versus all other groups, determined by two-way ANOVA. Scale bars, 50 mm. (B) Methodology used to assess the effect of WT and *ob/ob* ECMs on the disorganization of MCF10AT acini. Spreading was analyzed by measuring acini surface area and height. (C) Confocal image analysis of surface area and height of acini and representative confocal micrographs of intact versus spread MCF10A acini ($n = 100$ acini per condition). Horizontal lines indicate means. Scale bar, 50 mm. (D) Time-lapse imaging of MCF10AT migration on *ob/ob* relative to WT ECMs. (i) Representative image sequence visualizing MCF10AT migration along fibronectin fibers. Scale bar, 20 mm. (ii) *x-y* coordinate maps tracking individual cells over 300 min. (iii) Computed MCF10AT motility from (ii) ($n = 41$ cells per condition). Horizontal lines indicate means. *P* values in (C) and (D) determined by unpaired two-tailed *t* tests. FOV, field of view.

Obesity-associated ECM remodeling also occurs in human breast tissues

To determine the clinical relevance of our findings in mice and in vitro with human cell lines, we analyzed tumor-free breast tissue from normal, overweight, and obese patients. Specimens were derived from a previously published cohort of patients undergoing mastectomy (*37*) and were collected from either the contralateral breast or from parts not involved by the tumor to ensure that only noncancerous breast tissue was analyzed. a-SMA levels were increased in obese human breast tissue (Fig. 6A), and SHG imaging indicated a corresponding increase in collagen fiber aligned length (Fig. 6B).

Consistent with in vitro results (fig. S5), a-SMA levels in these tissues did not correlate with TGF-b expression, but did with obesity-associated ECM remodeling such as the amount of deposited fibronectin and collagen fiber thickness; a trend, but no statistical significance was noted for collagen fiber aligned length. In addition, a-SMA levels positively correlated with inflammation [indicated by crown-like structure of the breast (CLS-B) index] (Fig. 6C), confirming results from others that macrophage-derived factors may in part contribute to the increased levels of ECM remodeling in obese mice (*38*). The integrated effects of several obesity-associated parameters may therefore be necessary to accurately predict the risk of obesity-associated protumorigenic matrix remodeling.

Additionally, we analyzed desmoplastic remodeling in breast cancer specimens collected from lean and obese women. Pathological scoring of H&E-stained

cross sections of varied subtypes (table S1) revealed that tumors from obese patients exhibited more severe desmoplasia relative to tumors from lean patients (Fig. 7A, fig. S7, and table S1). Immunofluorescence analysis confirmed increased levels of a-SMA$^+$ cells and fibronectin in samples from obese patients compared with lean ones (Fig. 7, B and C). Moreover, obesity induces collagen-dependent structural changes that likely contribute to enhanced mechanical rigidity because samples from obese patients exhibited an increase not only in collagen fiber thickness but also in fiber aligned length (Fig. 7D).

Lastly, we confirmed that the differential ECM properties of obese human tumors correlated with enhanced mechanotransduction. In agreement with our in vitro results (Fig. 4D), the epithelial compartment of tumors from obese patients not only exhibited elevated overall levels of YAP/TAZ but also greater nuclear accumulation relative to tumors from lean patients (Fig. 7E). The detected changes in obesity-associated ECM remodeling may thus correspond to elevated mechanosignaling in obese tumors and play a key role in the worse clinical prognosis of obese cancer patients (*18*).

In a larger cohort, we performed bioinformatic analysis of genes differentially expressed in estrogen receptor–positive (ER$^+$) breast cancer in obese and nonobese patients (*39*). Consistent with our findings that obesity promotes ECM-dependent mechanotransduction, which correlates with inflammation, we found that obesity leads to enrichment of functional pathways associated with ECM-, adhesion-, and inflammation-related gene signatures in breast cancer patients (table S2). Further analysis of these obesity-associated, ECM-related (n = 49), and inflammation-related (n = 13) genes revealed a subset of eight genes common to both pathways (Fig. 7F). These eight genes were checked for coexpression with the other ECM-specific genes that were not common to the ECM- and inflammation-related subset, to understand their interaction with the other genes in the ECM pathway. This analysis indicates a strong correlation between ECM- and inflammation-related genes in obese ER$^+$ breast cancer patients showing that the eight genes were significantly coexpressed with other ECM-related genes [false discovery rate (FDR) < 0.2]. Moreover, expression of two YAP/TAZ-regulated genes (*CTGF* and *ANKRD)* (*34*), identified from a previously described ECM density–based gene signature (*7*), were correlated significantly (FDR < 0.2) with a subset of these eight genes, suggesting a possible co-regulation between obesity, mechanotransduction, ECM, and inflammation in ER$^+$ breast cancer patients (tables S2 and S3).

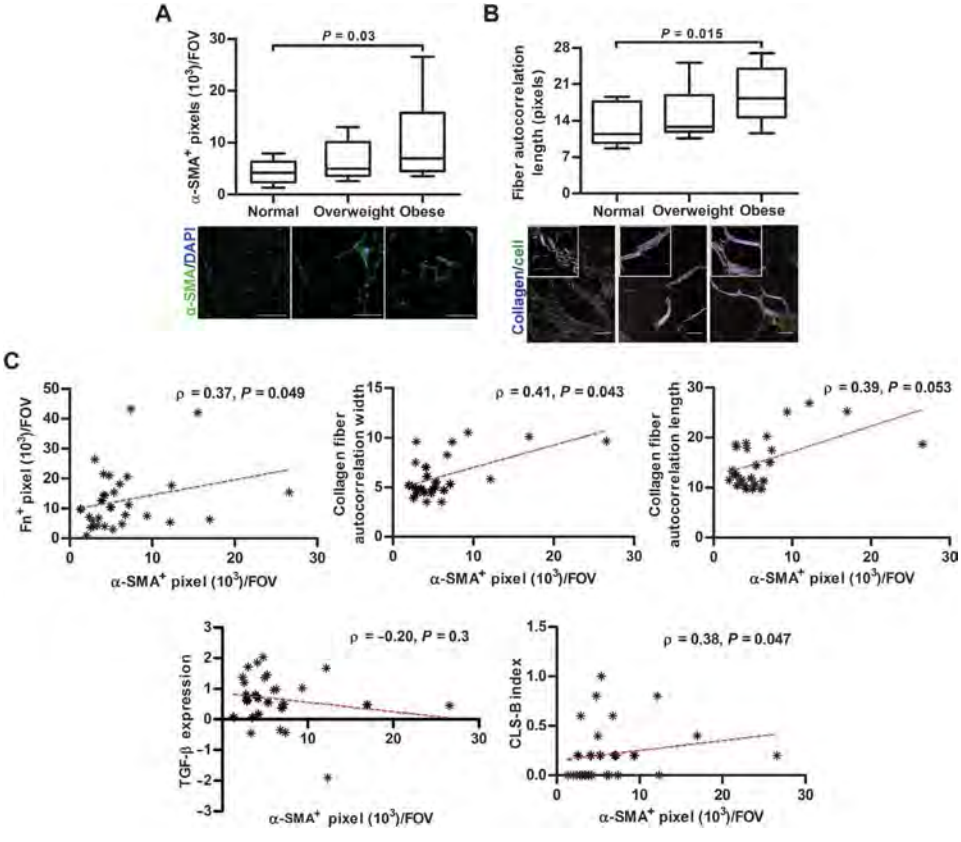

Fig. 6. Obesity-associated, tumor-free human breast tissue displays profibrotic features. (A and B) Immunofluorescence analysis of a-SMA levels (A) and SHG image analysis of collagen fibers (B) in tumor-free breast tissue from normal, overweight, and obese women. Scale bar, 100 mm (A); 50 mm (B). Data are medians with minimum and maximum values from 9 to 11 samples per group. *P* values by one-way ANOVA. (C) Correlation of a-SMA levels with fibronectin levels (determined by immunofluorescence), collagen fiber thickness and length (analyzed by SHG), TGF-b expression (measured by quantitative reverse transcriptase polymerase chain reaction), and obesity-associated chronic inflammation (as defined by CLS-B index). Spearman's rank correlation was used to determine *P* values, and its coefficient was denoted as rho (r). Data points represent individual samples (n = 28).

Caloric restriction decreases fibrotic features in mammary fat of obese mice

The therapeutic value of elective weight loss is unresolved at both the clinical and physiological levels, including the reversal of adipose tissue interstitial fibrosis (*16*, *40*). Therefore, we tested whether caloric restriction could reduce interstitial fibrosis in mammary fat. Ovariectomized mice were subjected to 10 weeks of high-fat diet to mimic postmenopausal obesity, followed by 7 weeks of caloric restriction to suppress further weight gain, according to our previous reports [22.1 ± 0.6 g (low-fat diet); 38.9 ± 2.2 g (high-fat diet); 30.1 ± 0.8 g (high-fat diet/caloric restriction)] (fig. S8A) (*41*). Caloric restriction reduced the content of myofibroblasts in mammary fat interstitial tissue; a similar, albeit not significant, trend was noted for fibronectin (fig. S8, B and C). These data suggest that caloric restriction can reverse features of fibrotic remodeling in mammary adipose tissue. However, longer-term follow-up will be required to determine whether these cellular changes translate to differences in ECM physicochemical properties and to extend this to clinical specimens.

DISCUSSION

Our results demonstrate that obesity leads to the formation of mechanical niches in adipose tissue that mimic characteristics of

tumor-associated stroma and promote carcinogenesis by altering mechanotransduction. More specifically, obesity increases the number of myofibroblasts in mammary adipose tissue, which, in turn, deposit a more fibrillar, partially unfolded, and stiffer ECM. This altered ECM not only provides a positive feedback mechanism for further myofibroblast differentiation but can also increase the malignant behavior of mammary epithelial cells. Collectively, our results suggest that altered ECM physicochemical properties not only are a hallmark of already established tumors but may also be responsible for the increased risk and worse clinical prognosis of obese breast cancer patients. The detected changes in obesity-associated ECM remodeling correlated with inflammation, a known hallmark of both tumorigenesis and obesity (*3*, *42*). Hence, our findings provide a new perspective on the tumor-promoting capability of inflammation (*2*).

Although obesity induces fibrosis in subcutaneous and visceral adipose tissue (*16*), our results show that similar changes also occur in mammary adipose tissue. This observation is important given that (i) the global functions and fibrotic remodeling of adipose tissue vary between anatomic depots (*4*, *16*) and (ii) the local microenvironment of the breast is indisputably relevant to mammary tumorigenesis (*43*). Obesity also caused fibrotic remodeling in mammary fat from ovariectomized mice, further suggesting that obesity-associated stiffening of the ECM occurs independently of hormone status and is therefore pertinent to both pre- and postmenopausal breast cancers. The levels of obesity-associated fibrotic remodeling were the same in control and ovariectomized mice, although the latter featured increased body weight and inflammation (*19*). Hence, it is possible that a threshold for inflammation-mediated fibrotic changes exists. Nevertheless, it is also conceivable that ovariectomy counterbalances some of the profibrotic effects mediated by obesity/inflammation because reduced estrogen levels can diminish fibrosis (*44*).

The described obesity-associated changes in ECM physicochemical characteristics were related to an increase of myofibroblasts (*11*), which elevated matrix stiffness consistent with previous reports, for instance, by increasing ECM quantity (*8*), collagen alignment (*45*), and fibronectin unfolding (*27*). Obesity-associated ECMs elevated ASC contractility and thus myofibroblast differentiation, a mechanism also reported for cancer-associated fibroblasts (*30*). Nevertheless, increased myofibroblast content in obese breast tissue may also arise from alternative mechanisms including increased recruitment of bone marrow mesenchymal cells (*46*) or altered adipocyte-macrophage crosstalk (*38*). In addition to changing ASC behavior, obesity-associated ECMs increased the malignant behavior of MDA-MB231 and premalignant MCF10AT human breast cancer cells. Hence, obesity-associated changes in breast adipose tissue interstitial stiffness not only promote aggression of already existing tumors but may also contribute to the transformation of early-stage breast cancer. This is particularly relevant because obese

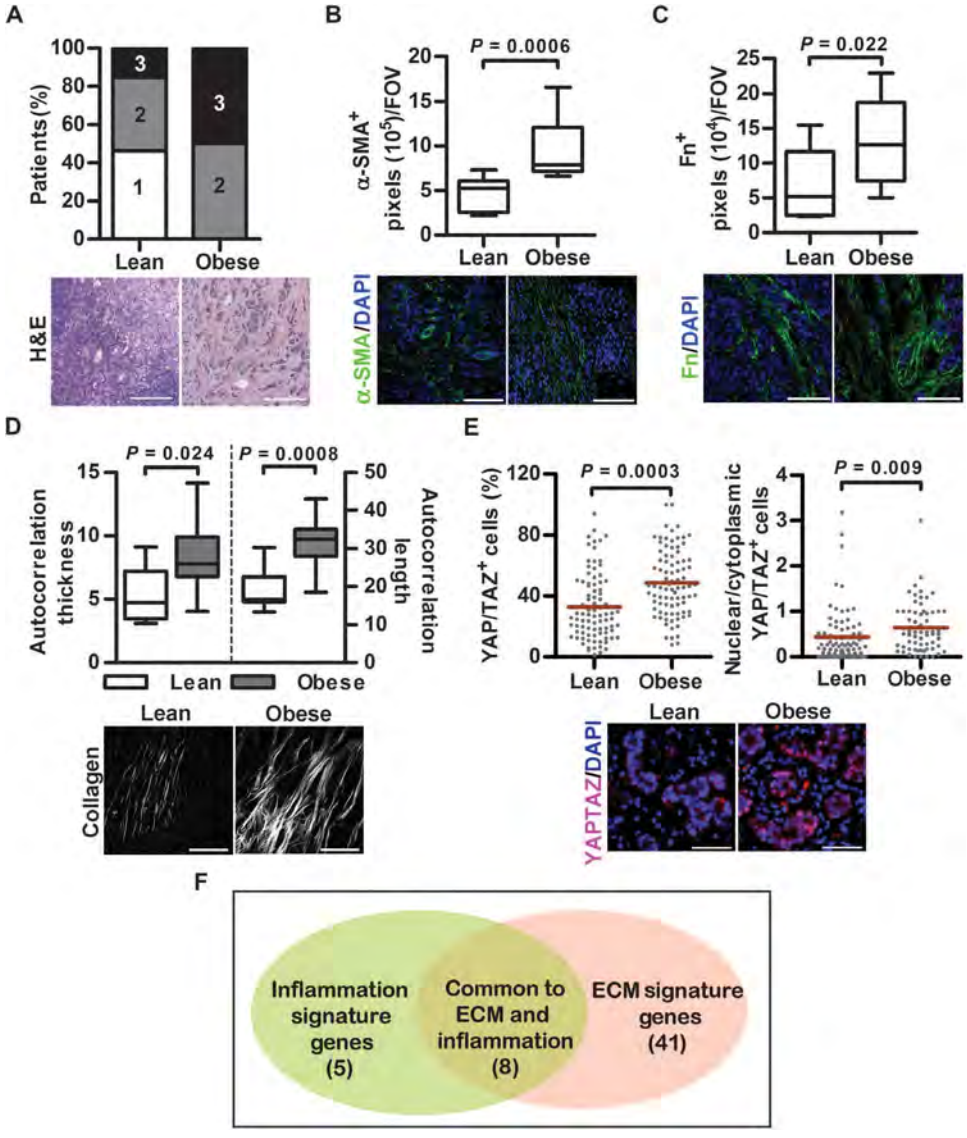

Fig. 7. Obesity-associated ECM remodeling in patient samples. (A) Histopathological scoring of clinical tumor specimens for degree (1 to 3) of desmoplasia (n = 17 to 18 patients per group). Scale bars, 200 mm. Statistical significance was assessed by Fisher's exact test. (B and C) Immunofluorescence analysis of a-SMA (B) and fibronectin (C) content in breast tumor specimens from obese and lean patients (n = 10 patients per group). (D) SHG image analysis of collagen fiber thickness and length. Data are medians with minimum and maximum values (n = 10 patients per group). P values in (B to D) were determined by Mann-Whitney U tests. (E) Immunofluorescence image analysis of epithelial total and nuclear YAP/TAZ in tumors. Data points are individual images (n =10 images per patient, 10 patients per group). P values by mixed-model design ANOVA. Scale bars, 100 mm. (F) Bioinformatics analysis of published data (*39*) to correlate obesity-induced transcriptomic changes with ECM- and inflammation-related gene signatures.

ASCs secrete enhanced levels of SDF-1–stimulating cellular recruitment to sites of protumorigenic ECM remodeling. However, whether different tumor subtypes may vary in their responsiveness to obesity-associated ECM changes should be confirmed with primary cells and patient samples stratified by tumor subtype.

Using specimens from lean and obese patients as well as testing the effect of caloric restriction on fibrotic remodeling of mammary fat, we provide experimental evidence supporting the clinical relevance of our results. We demonstrated not only that obesity promotes features of fibrotic remodeling in cancer-free breast tissue but also that obesity worsens desmoplasia and the related ECM changes in mammary tumors. Weight loss and exercise are routinely recommended for obese cancer patients because this regime may improve the clinical outcome of cancer patients (*47*). A number of possibilities including altered metabolism (*48*) and reduction of local inflammation may contribute to this end (*41*). Additionally, our data in obese, ovariectomized mice suggest that caloric restriction can reverse fibrotic remodeling; a similar trend was noted for ECM remodeling, although the effect may be delayed relative to cellular changes (*49*). Furthermore, the length of exposure to altered ECM physicochemical properties may influence the capability of ASC-derived myofibroblasts to lose their contractile phenotype in response to dietary intervention (*29*).

On the basis of our reported results, a number of questions arise. The initial obesity-associated mechanisms elevating ECM mechanics are yet unknown. Obesity-associated hypoxia may be responsible, given its ability to up-regulate collagen cross-linking and, thus, ECM stiffness (*13*, *50*). Alternatively, obesity-associated chronic inflammation may play a role. However, whether inflammation is the driver or rather a consequence of ECM remodeling remains to be confirmed. Our patient genetic data suggest a connection between obesity, ECM remodeling, inflammation, and mechanotransduction, but more patients will be necessary to discern the strength of this connection and whether inflammation contributes to increased stiffness of obese mammary fat and tumors. Moreover, obesity-associated fibrosis has been correlated with elevated levels of collagen type VI and its cleavage product, endotrophin (*4*). Whether the tumor-promoting effects of these factors may in part be related to altered ECM mechanics is unclear. Although we evaluated the direct effect of obesity-mediated ECM differences on ASCs and tumor cells, altered ECM mechanics can indirectly promote tumorigenesis, for instance, by influencing soluble factor (for example, adipokines) signaling and other stromal cell responses (*2*, *27*, *33*).

Other than caloric restriction, there are several clinically relevant aspects to our study. Mammography is commonly used for early detection of breast cancer and overall risk assessment because women with mammographically dense breasts have a higher probability of developing breast cancer. However, because fat is radiolucent, obese women appear to have nondense breast tissue (*51*), although our data suggest that local, microscale density changes still occur. Therefore, alternative high-resolution imaging will be necessary to better localize and monitor regions that may stimulate tumorigenesis in obese patients. Furthermore, adipose tissue or ASCs are increasingly being considered for regenerative approaches to mastectomy. Thus far, little attention has been given to the body habitus of the patient from whom the ASCs are isolated, yet our data imply that ASCs from obese individuals might promote recurrence of breast cancer relative to ASCs from lean patients. Stratification of patients on the basis of obesity-associated features may help to better assess the potential risk, if any, associated with adipose tissue–based reconstructive approaches (*52*). Together, our results are of broad relevance to the field of obesity-induced cancer and inform a multitude of future opportunities in the arena of physical sciences in oncology.

MATERIALS AND METHODS

Study design

This study was designed to investigate the hypothesis that obesity-associated fibrosis promotes breast cancer malignancy by altering mechanotransduction. In vitro and in vivo experiments were performed to analyze obesity-associated ECM physicochemical properties. Tumor cell responses to lean and obese ECMs were tested in vitro and confirmed with patient samples. All clinical samples were obtained from patients with varying demographic background and were stratified on the basis of body mass index. Sample sizes for analysis of mouse and cancer-free human samples were based on our previous studies (*37*). Sample sizes for analysis of clinical tumor samples were chosen to detect a statistical significance of $P < 0.05$. For all in vitro studies, three independent experiments with at least three samples per condition were performed. Outliers were not excluded, but data from human breast tumors were transformed by either log or square root before statistical analysis. Histomorphometric analysis of mouse and patient samples was blinded; in vitro experiments were not blinded.

Cell isolation and culture

ASCs were isolated from the stromal vascular fraction of either inguinal (a mix of subcutaneous and mammary) or visceral white fat of both genetic (11-week-old) and dietary (15-week-old) mouse models via collagenase digestion and density centrifugation (Fig. 2A) (*53*), as described further in the Supplementary Methods.

Analysis of mammary tissue and cellular behavior

Differences in obesity-associated breast tissue remodeling and corresponding changes in cellular behavior were assessed with cultured cells and ex vivo mammary tissue by immunostaining, FRET and SHG image analysis, Western blot, and SFA and AFM measurements as described in the Supplementary Methods. Ex vivo mammary tissues (murine mammary fat pads, tumor-free human breast tissue, and human breast tumor specimens) were isolated as described in the Supplementary Methods.

Statistical analysis

Microsoft Excel, GraphPad Prism 5, and JMP 11 were used for statistical analysis. Unless otherwise noted, unpaired Student's t tests and ANOVA with post hoc Tukey's test were used to compare parametric data between two conditions and among multiple conditions, respectively. Results were also confirmed with the Mann-Whitney U test and the Wilcoxon signed-rank test, respectively. Statistical correlation between the nonparametric variables of human breast tissue was assessed by Spearman's rank correlation, and its coefficient was denoted as rho (r). The effect of obesity on human tumor samples (table S1) was tested by Fisher's exact test. Two-sided testing with normal-based 95% confidence interval was performed for each analysis, and $P < 0.05$ was considered statistically significant. In vitro results are shown for one representative study after similar results were replicated in three separate experiments. An independent statistician was consulted for all statistical analyses.

SUPPLEMENTARY MATERIALS

REFERENCES AND NOTES

1. S. Hefetz-Sela, P. E. Scherer, Adipocytes: Impact on tumor growth and potential sites for therapeutic intervention. *Pharmacol. Ther.* 138, 197–210 (2013).
2. M. J. Khandekar, P. Cohen, B. M. Spiegelman, Molecular mechanisms of cancer development in obesity. *Nat. Rev. Cancer* 11, 886–895 (2011).
3. C. Henegar, J. Tordjman, V. Achard, D. Lacasa, I. Cremer, M. Guerre-Millo, C. Poitou, A. Basdevant, V. Stich, N. Viguerie, D. Langin, P. Bedossa, J. D. Zucker, K. Clemen, Adipose tissue transcriptomic signature highlights the pathological relevance of extracellular matrix in human obesity. *Genome Biol.* 9, R14 (2008).
4. J. Park, P. E. Scherer, Adipocyte-derived endotrophin promotes malignant tumor progression. *J. Clin. Invest.* 122, 4243–4256 (2012).
5. J. Schrader, T. T. Gordon-Walker, R. L. Aucott, M. van Deemter, A. Quaas, S. Walsh, D. Benten, S. J. Forbes, R. G. Wells, J. P. Iredale, Matrix stiffness modulates proliferation, chemotherapeutic response, and dormancy in hepatocellular carcinoma cells. *Hepatology* 53, 1192–1205 (2011).
6. M. Egeblad, M. G. Rasch, V. M. Weaver, Dynamic interplay between the collagen scaffold and tumor evolution. *Curr. Opin. Cell Biol.* 22, 697–706 (2010).
7. P. P. Provenzano, D. R. Inman, K. W. Eliceiri, P. J. Keely, Matrix density-induced mechanoregulation of breast cell phenotype, signaling and gene expression through a FAK-ERK linkage. *Oncogene* 28, 4326–4343 (2009).
8. M. J. Paszek, N. Zahir, K. R. Johnson, J. N. Lakins, G. I. Rozenberg, A. Gefen, C. A. Reinhart-King, S. S. Margulies, M. Dembo, D. Boettiger, D. A. Hammer, V. M. Weaver, Tensional homeostasis and the malignant phenotype. *Cancer Cell* 8, 241–254 (2005).
9. A. Mammoto, K. M. Connor, T. Mammoto, C. W. Yung, D. Huh, C. M. Aderman, G. Mostoslavsky, L. E. Smith, D. E. Ingber, A mechanosensitive transcriptional mechanism that controls angiogenesis. *Nature* 457, 1103–1108 (2009).
10. A. J. Engler, S. Sen, H. L. Sweeney, D. E. Discher, Matrix elasticity directs stem cell lineage specification. *Cell* 126, 677–689 (2006).
11. E. M. Chandler, B. R. Seo, J. P. Califano, R. C. Andresen Eguiluz, J. S. Lee, C. J. Yoon, D. T. Tims, J. X. Wang, L. Cheng, S. Mohanan, M. R. Buckley, I. Cohen, A. Y. Nikitin, R. M. Williams, D. Gourdon, C. A. Reinhart-King, C. Fischbach, Implanted adipose progenitor cells as physicochemical regulators of breast cancer. *Proc. Natl. Acad. Sci. U.S.A.* 109, 9786–9791 (2012).
12. J. J. Tomasek, G. Gabbiani, B. Hinz, C. Chaponnier, R. A. Brown, Myofibroblasts and mechano-regulation of connective tissue remodelling. *Nat. Rev. Mol. Cell Biol.* 3, 349–363 (2002).
13. K. R. Levental, H. Yu, L. Kass, J. N. Lakins, M. Egeblad, J. T. Erler, S. F. Fong, K. Csiszar, A. Giaccia, W. Weninger, M. Yamauchi, D. L. Gasser, V. M. Weaver, Matrix crosslinking forces tumor progression by enhancing integrin signaling. *Cell* 139, 891–906 (2009).
14. H. Yadav, C. Quijano, A. K. Kamaraju, O. Gavrilova, R. Malek, W. Chen, P. Zerfas, D. Zhigang, E. C. Wright, C. Stuelten, P. Sun, S. Lonning, M. Skarulis, A. E. Sumner, T. Finkel, S. G. Rane, Protection from obesity and diabetes by blockade of TGF-b/Smad3 signaling. *Cell Metab.* 14, 67–79 (2011).
15. M. C. Vohl, R. Sladek, J. Robitaille, S. Gurd, P. Marceau, D. Richard, T. J. Hudson, A. Tchernof, A survey of genes differentially expressed in subcutaneous and visceral adipose tissue in men. *Obes. Res.* 12, 1217–1222 (2004).
16. A. Divoux, J. Tordjman, D. Lacasa, N. Veyrie, D. Hugol, A. Aissat, A. Basdevant, M. Guerre-Millo, C. Poitou, J.-D. Zucker, P. Bedossa, K. Clément, Fibrosis in human adipose tissue: Composition, distribution, and link with lipid metabolism and fat mass loss. *Diabetes* 59, 2817–2825 (2010).
17. Y. Zhang, R. Proenca, M. Maffei, M. Barone, L. Leopold, J. M. Friedman, Positional cloning of the mouse *obese* gene and its human homologue. *Nature* 372, 425–432 (1994).
18. E. E. Calle, R. Kaaks, Overweight, obesity and cancer: Epidemiological evidence and proposed mechanisms. *Nat. Rev. Cancer* 4, 579–591 (2004).
19. K. Subbaramaiah, L. R. Howe, P. Bhardwaj, B. Du, C. Gravaghi, R. K. Yantiss, X. K. Zhou, V. A. Blaho, T. Hla, P. Yang, L. Kopelovich, C. A. Hudis, A. J. Dannenberg, Obesity is associated with inflammation and elevated aromatase expression in the mouse mammary gland. *Cancer Prev. Res.* 4, 329–346 (2011).
20. M. W. Conklin, J. C. Eickhoff, K. M. Riching, C. A. Pehlke, K. W. Eliceiri, P. P. Provenzano, A. Friedl, P. J. Keely, Aligned collagen is a prognostic signature for survival in human breast carcinoma. *Am. J. Pathol.* 178, 1221–1232 (2011).
21. A. Orimo, R. A. Weinberg, Stromal fibroblasts in cancer: A novel tumor-promoting cell type. *Cell Cycle* 5, 1597–1601 (2006).
22. H. P. Ehrlich, T. M. Krummel, Regulation of wound healing from a connective tissue perspective. *Wound Repair Regen.* 4, 203–210 (1996).
23. F. Shi, J. Harman, K. Fujiwara, J. Sottile, Collagen I matrix turnover is regulated by fibronectin polymerization. *Am. J. Physiol. Cell Physiol.* 298, C1265–C1275 (2010).
24. K. E. Kadler, A. Hill, E. G. Canty-Laird, Collagen fibrillogenesis: Fibronectin, integrins, and minor collagens as organizers and nucleators. *Curr. Opin. Cell Biol.* 20, 495–501 (2008).
25. P. Singh, C. Carraher, J. E. Schwarzbauer, Assembly of fibronectin extracellular matrix. *Annu. Rev. Cell Dev. Biol.* 26, 397–419 (2010).
26. E. M. Chandler, M. P. Saunders, C. J. Yoon, D. Gourdon, C. Fischbach, Adipose progenitor cells increase fibronectin matrix strain and unfolding in breast tumors. *Phys. Biol.* 8, 015008 (2011).
27. K. Wang, R. C. Andresen Eguiluz, F. Wu, B. R. Seo, C. Fischbach, D. Gourdon, Stiffening and unfolding of early deposited-fibronectin increase proangiogenic factor secretion by breast cancer-associated stromal cells. *Biomaterials* 54, 63–71 (2015).
28. A. Krammer, D. Craig, W. E. Thomas, K. Schulten, V. Vogel, A structural model for force regulated integrin binding to fibronectin's RGD-synergy site. *Matrix Biol.* 21, 139–147 (2002).
29. J. L. Balestrini, S. Chaudhry, V. Sarrazy, A. Koehler, B. Hinz, The mechanical memory of lung myofibroblasts. *Integr. Biol.* 4, 410–421 (2012).
30. F. Calvo, N. Ege, A. Grande-Garcia, S. Hooper, R. P. Jenkins, S. I. Chaudhry, K. Harrington, P. Williamson, E. Moeendarbary, G. Charras, E. Sahai, Mechanotransduction and YAP-dependent matrix remodelling is required for the generation and maintenance of cancer-associated fibroblasts. *Nat. Cell Biol.* 15, 637−646 (2013).
31. L. Buscemi, D. Ramonet, F. Klingberg, A. Formey, J. Smith-Clerc, J.J. Meister, B. Hinz, The single-molecule mechanics of the latent TGF-b1 complex. *Curr. Biol.* 21, 2046–2054 (2011).
32. J. C. Friedland, M. H. Lee, D. Boettiger, Mechanically activated integrin switch controls a_5b_1 function. *Science* 323, 642–644 (2009).
33. P. P. Provenzano, P. J. Keely, Mechanical signaling through the cytoskeleton regulates cell proliferation by coordinated focal adhesion and Rho GTPase signaling. *J. Cell Sci.* 124, 1195–1205 (2011).
34. S. Dupont, L. Morsut, M. Aragona, E. Enzo, S. Giulitti, M. Cordenonsi, F. Zanconato, J. Le Digabel, M. Forcato, S. Bicciato, N. Elvassore, S. Piccolo, Role of YAP/TAZ in mechanotransduction. *Nature* 474, 179–183 (2011).
35. J. Debnath, S. K. Muthuswamy, J. S. Brugge, Morphogenesis and oncogenesis of MCF-10A mammary epithelial acini grown in three-dimensional basement membrane cultures. *Methods* 30, 256–268 (2003).
36. O. Chaudhuri, S. T. Koshy, C. Branco da Cunha, J.-W. Shin, C. S. Verbeke, K. H. Allison, D. J. Mooney, Extracellular matrix stiffness and composition jointly regulate the induction of malignant phenotypes in mammary epithelium. *Nat. Mater.* 13, 970–978 (2014).
37. P. G. Morris, C. A. Hudis, D. Giri, M. Morrow, D. J. Falcone, X. K. Zhou, B. Du, E. Brogi, C. B. Crawford, L. Kopelovich, K. Subbaramaiah, A. J. Dannenberg, Inflammation and increased aromatase expression occur in the breast tissue of obese women with breast cancer. *Cancer Prev. Res.* 4, 1021–1029 (2011).
38. M. Tanaka, K. Ikeda, T. Suganami, C. Komiya, K. Ochi, I. Shirakawa, M. Hamaguchi, S. Nishimura, I. Manabe, T. Matsuda, K. Kimura, H. Inoue, Y. Inagaki, S. Aoe, S. Yamasaki, Y. Ogawa, Macrophage-inducible C-type lectin underlies obesity-induced adipose tissue fibrosis. *Nat. Commun.* 5, 4982 (2014).
39. E. Fuentes-Mattei, G. Velazquez-Torres, L. Phan, F. Zhang, P.-C. Chou, J.-H. Shin, H. H. Choi, J.-S. Chen, R. Zhao, J. Chen, C. Gully, C. Carlock, Y. Qi, Y. Zhang, Y. Wu, F. J. Esteva, Y. Luo, W. L. McKeehan, J. Ensor, G. N. Hortobagyi, L. Pusztai, W. Fraser Symmans, M.-H. Lee, S.-C. Yeung, Effects of obesity on transcriptomic changes and cancer hallmarks in estrogen receptor-positive breast cancer. *J. Natl. Cancer Inst.* 106, dju158 (2014).
40. R. Cancello, A. Zulian, D. Gentilini, M. Mencarelli, A. Della Barba, M. Maffei, P. Vitti, C. Invitti, A. Liuzzi, A. M. Di Blasio, Permanence of molecular features of obesity in subcutaneous adipose tissue of ex-obese subjects. *Int. J. Obes.* 37, 867–873 (2013).
41. P. Bhardwaj, B. Du, X. K. Zhou, E. Sue, M. D. Harbus, D. J. Falcone, D. Giri, C. A. Hudis, L. Kopelovich, K. Subbaramaiah, A. J. Dannenberg, Caloric restriction reverses obesity-induced mammary gland inflammation in mice. *Cancer Prev. Res.* 6, 282–289 (2013).

42. S. I. Grivennikov, F. R. Greten, M. Karin, Immunity, inflammation, and cancer. *Cell* 140, 883–899 (2010).
43. M. J. Bissell, D. C. Radisky, A. Rizki, V. M. Weaver, O. W. Petersen, The organizing principle: Microenvironmental influences in the normal and malignant breast. *Differentiation* 70, 537–546 (2002).
44. M. Nielsen, P. C. Pettersen, P. Alexandersen, G. Karemore, J. Raundahl, M. Loog, C. Christiansen, Breast density changes associated with postmenopausal hormone therapy: Post hoc radiologist- and computer-based analyses. *Menopause* 17, 772–778 (2010).
45. K. M. Riching, B. L. Cox, M. R. Salick, C. Pehlke, A. S. Riching, S. M. Ponik, B. R. Bass, W. C. Crone, Y. Jiang, A. M. Weaver, K. W. Eliceiri, P. J. Keely, 3D collagen alignment limits protrusions to enhance breast cancer cell persistence. *Biophys. J.* 107, 2546–2558 (2014).
46. N. C. Direkze, S. J. Forbes, M. Brittan, T. Hunt, R. Jeffery, S. L. Preston, R. Poulsom, K. Hodivala-Dilke, M. R. Alison, N. A. Wright, Multiple organ engraftment by bone-marrow-derived myofibroblasts and fibroblasts in bone-marrow-transplanted mice. *Stem Cells* 21, 514–520 (2003).
47. K. Y. Wolin, K. Carson, G. A. Colditz, Obesity and cancer. *Oncologist* 15, 556–565 (2010).
48. V. D. Longo, L. Fontana, Calorie restriction and cancer prevention: Metabolic and molecular mechanisms. *Trends Pharmacol. Sci.* 31, 89–98 (2010).
49. Y. Higami, J. L. Barger, G. P. Page, D. B. Allison, S. R. Smith, T. A. Prolla, R. Weindruch, Energy restriction lowers the expression of genes linked to inflammation, the cytoskeleton, the extracellular matrix, and angiogenesis in mouse adipose tissue. *J. Nutr.* 136, 343–352 (2006).
50. N. Halberg, T. Khan, M. E. Trujillo, I. Wernstedt-Asterholm, A. D. Attie, S. Sherwani, Z. V. Wang, S. Landskroner-Eiger, S. Dineen, U. J. Magalang, R. A. Brekken, P. E. Scherer, Hypoxia-inducible factor 1a induces fibrosis and insulin resistance in white adipose tissue. *Mol. Cell. Biol.* 29, 4467–4483 (2009).
51. J. Peres, Understanding breast density and breast cancer risk. *J. Natl. Cancer Inst.* 104, 1345–1346 (2012).
52. F. Bertolini, V. Lohsiriwat, J.-Y. Petit, M. G. Kolonin, Adipose tissue cells, lipotransfer and cancer: A challenge for scientists, oncologists and surgeons. *Biochim. Biophys. Acta* 1826, 209–214 (2012).
53. A. C. Boquest, A. Shahdadfar, J. E. Brinchmann, P. Collas, Isolation of stromal stem cells from human adipose tissue. *Methods Mol. Biol.* 325, 35–46 (2006).
54. R. M. Williams, A. Flesken-Nikitin, L. H. Ellenson, D. C. Connolly, T. C. Hamilton, A. Y. Nikitin, W. R. Zipfel, Strategies for high-resolution imaging of epithelial ovarian cancer by laparoscopic nonlinear microscopy. *Transl. Oncol.* 3, 181–194 (2010).
55. M. L. Smith, D. Gourdon, W. C. Little, K. E. Kubow, R. A. Eguiluz, S. Luna-Morris, V. Vogel, Force-induced unfolding of fibronectin in the extracellular matrix of living cells. *PLOS Biol.* 5, e268 (2007).
56. R. Castelló-Cros, E. Cukierman, Stromagenesis during tumorigenesis: Characterization of tumor-associated fibroblasts and stroma-derived 3D matrices. *Methods Mol. Biol.* 522, 275–305 (2009).
57. K. L. Johnson, *Contact Mechanics* (Cambridge Univ. Press, 1985).
58. D. W. Huang, B. T. Sherman, R. A. Lempicki, Systematic and integrative analysis of large gene lists using DAVID bioinformatics resources. *Nat. Protoc.* 4, 44–57 (2009).

Acknowledgments: We thank M. Paszek and V. Weaver for helpful discussions; F. Vermeylen for consultation on statistical analysis; L. Yang, H. Sha, and L. Qi for the adipose tissue for preliminary studies; N. Springer for proofreading; Cornell's Center for Animal Resources and Education, the Imaging Facilities of Cornell's Biotechnology Resource Center (BRC), and Cornell's Center for Materials Research (CCMR). Funding: This study was funded by NIH/NCI (National Cancer Institute) [U54CA143876, R01CA185293, R01CA154481, R21CA161532, 1S10RR025502, and S10OD010605 (BRC)], the National Science Foundation [CMMI 1031068, DMR-1120296 (CCMR)], the Breast Cancer Research Foundation, the Botwinick-Wolfensohn Foundation (in memory of Mr. and Mrs. Benjamin Botwinick), and 2UL1TR000457-06 of the Clinical and Translational Science Center at Weill Cornell Medical College. Author contributions: B.R.S. performed all experiments unless otherwise noted; P.B. generated mouse samples; S.C. performed AFM measurements; J.G. aided mouse sample image analysis; R.C.A.E. and D.G. performed SFA measurements; K.W. and D.G. prepared FRET-labeled fibronectin; S.M. performed histophathological assessment; R.M.W. helped with the SHG analysis; L.T.V. collected tumor specimens; A.V. and O.E. performed bioinformatics analysis; P.G.M. and C.A.H. collected tumor-free breast tissue; B.D. and X.K.Z. performed gene expression analysis; B.R.S., J.G., R.C.A.E., S.C., A.V., O.E., R.M.W., D.G., A.J.D., and C.F. analyzed the data; B.R.S., and C.F. wrote the paper; B.R.S., A.J.D., and C.F. designed the study. All authors were involved in the discussion of results and critical reading of the manuscript. Competing interests: The authors declare that they have no competing interests. Data and materials availability: All data and materials are available.

Supplementary Materials for

Obesity-dependent changes in interstitial ECM mechanics promote breast tumorigenesis

Bo Ri Seo, Priya Bhardwaj, Siyoung Choi, Jacqueline Gonzalez, Roberto C. Andresen Eguiluz, Karin Wang, Sunish Mohanan, Patrick G. Morris, Baoheng Du, Xi K. Zhou, Linda T. Vahdat, Akanksha Verma, Olivier Elemento, Clifford A. Hudis, Rebecca M. Williams, Delphine Gourdon, Andrew J. Dannenberg, Claudia Fischbach

This Supplementary Materials' File includes:

Supplementary Materials

Materials and Methods

Animal models and tissue isolation

To characterize obesity-associated interstitial fibrosis mammary, inguinal, or visceral fat was isolated from both dietary and genetic mouse models of obesity (n = 10/group). For the dietary model, female 5 week-old C57BL/6J mice (Jackson Laboratories) were randomized and fed low fat diet (LFD) or high fat diet (HFD) (Research Diets: D12492i, 10 kcal% fat and 12450Bi, 60 kcal% fat, respectively) *ad libitum* for 10 weeks as previously described (Fig. 1A) (*19*). For the genetic model, 8 week-old B6.Cg-Lep^{ob}/J (*ob/ob*) and their age-matched C57BL/6J wild-type controls (Jackson Laboratories) were fed PicoLab Rodent Diet 20, #5053 (W.F. Fisher & Son) *ad libitum* until sacrifice at 11 weeks of age (Fig. 1A). In the dietary model, to mimic menopause, either ovariectomy (OVX) or sham surgery was performed on C57BL/6J mice at 4 weeks of age. One week post-surgery, ovariectomized (OVX) and ovary intact mice were randomized for dietary intervention (LFD or HFD) (fig. S1A). To study the effect of caloric restriction, OVX mice received 10 weeks of HFD feeding and were subsequently subjected to 30% caloric restriction (CR) for 7 weeks using previously established protocols (fig. S8A) (*41*). Age-matched control mice were fed LFD or HFD for a total of 17 weeks (n = 6/group). Isolated tissues were formalin fixed for immunohistochemical evaluation, or frozen and stored at -80°C for subsequent biochemical analysis. Animal protocols were approved by the Institutional Animal Care and Use Committees at Weill Cornell Medical College and Cornell University.

Cell isolation and culture

ASCs were isolated from the stromal vascular fraction of either inguinal (a mix of s.c. and mammary) or visceral white fat of both genetic (11 week-old) and dietary (15 week- old) mouse models via collagenase digestion and density centrifugation (Fig. 2A) (*53*). Briefly, isolated tissue was minced in Krebs-Ringer-HEPES (*KRBH*) *buffer* prepared as described previously and digested with 1.5 mg/ml collagenase type 1 buffer (Worthington Biochemical Corp.). Digested tissue was filtered through a 250-μm cell strainer (Pierce) and centrifuged in Histopaque-1077 solution (Sigma) to separate ASCs from adipocytes. Isolated ASCs were cultured in media containing 1:1 Dulbecco's Modified Eagle Medium (DMEM)/F12 (Gibco) supplemented with 10% FBS (Tissue Culture Biologicals), 1% antibiotic (penicillin/streptomycin) (Gibco), up to passage 4. Human MDA-MB231 breast cancer cells (ATCC) were cultured in αMEM (Sigma) containing 10% FBS and 1% antibiotic. MCF10AT (Barbara Ann Karmanos Cancer Institute) were cultured in DMEM/F12 (Gibco) supplemented with EGF (20 ng/ml) (Millipore), hydrocortisone (500 μg/ml) (Sigma-Aldrich), cholera toxin (100 ng/ml) (Sigma-Aldrich), insulin (10 μg/ml) (Sigma-Aldrich), 5% horse serum (Gibco), and 1% antibiotic.

Mammary tissue immunostaining and image analysis

Cross-sections were prepared from paraffin-embedded mammary fat and subjected to H&E staining and IF (for fibronectin [Fn] and α-SMA). Antigen retrieval was performed with 0.1-M citrate buffer, pH 6.0 (for α-SMA IF), and additional proteinase K treatment (for Fn IF) (Dako). Subsequently, tissue sections were permeabilized and blocked with SuperBlock (Thermo Fisher) in 0.05% Tween-20 PBS (PBST). For α-SMA staining,

M.O.M kit blocking reagent (Vector Laboratories) was used. After overnight incubation (4°C) with primary antibodies against Fn (Sigma-Aldrich) or α-SMA (Invitrogen), sections were incubated with AlexaFluor 488-conjugated secondary antibody, counterstained with 4',6-diamidino-2-phenylindole (DAPI), and then mounted with Prolong Gold reagent (all from Invitrogen). For each sample, 10 to 20 randomly selected areas (excluding mammary epithelial structures) were imaged with a Zeiss Observer Z.1 microscope and an AxioCam MRm camera, and average fluorescence intensity was calculated. For α-SMA analysis, α-SMA associated with glands and vasculature structures was excluded. To correct for background, all images were thresholded by subtracting fluorescence intensity of negative controls using Adobe Photoshop (n = 10 samples/group). The isolated positive pixels of each image were quantified in ImageJ (NIH) and then normalized to the number of adipocytes.

Characterization of collagen fibers by SHG imaging analysis

Multiphoton SHG imaging was used to characterize collagen structure in fresh mammary tissue (genetic mouse model) and rehydrated cross-sections of paraffin-embedded mammary tissue (dietary mouse model, human tumor-free breast tissue, human breast tumors). Imaging was performed with a custom-built multiphoton microscope using 780-nm illumination and an Olympus 20x/0.95W XLUMPlanFl objective (*54*). Emissions were separated into SHG (360-405 nm, pseudocolored purple) and autofluorescence (420-550 nm, pseudocolored green) channels. For murine samples, mammary tissue from 11 week-old *ob/ob* and lean mice (n = 3 samples/condition) was isolated and immersed in PBS. Z-stacks (50-120 μm in depth) of areas adjacent to the mammary epithelium, as

identified in transmitted light mode, were acquired at 2-μm intervals; 5 to 6 locations per tissue were imaged. For mammary tissue from the dietary mouse model of obesity and human specimens, 4-μm cross-sections were deparaffinized, rehydrated, and immersed in PBS. Micrographs of 10 regions per sample were collected and a total of 10 specimens per condition were analyzed. SHG channel images were extracted and analyzed through a custom-built autocorrelation analysis algorithm as previously described (*54*). To analyze collagen structure, a 2D spatial autocorrelation was computed from the SHG channel image. An autocorrelation ellipse was generated by fitting to 1/e of the maximum value of each image autocorrelation; the mean radius of the ellipse (in pixels) indicates the length scale of the collagen framework. The minimum and maximum radius of the ellipse were obtained and presented as the correlation thickness and correlation length of the fibers, respectively. The correlation thickness and length suggest the thickness and aligned length of collagen fibers, respectively. The linearity was determined by calculating the ratio of maximum to minimum radius of the ellipse, and this indicates the linearity of collagen fibers.

Characterization of isolated ASCs

Isolated ASCs were plated on glass coverslips, cultured for 3 to 5 days, fixed with 4% paraformaldehyde (PFA), and then immunofluorescently analyzed for α-SMA, proliferative capacity, and ECM deposition. To determine proliferation, ASCs were incubated with 10 μM bromodeoxyuridine (BrdU) (Sigma-Aldrich) for 20 hours. After fixation, cells were pretreated with ice-cold 1-N HCl, 37°C 2-N HCl, and 0.1-M borate buffer; incubated with biotinylated mouse anti-BrdU (Invitrogen); and, finally,

fluorescently labeled with streptavidin-conjugated AlexaFluor 555. For IF of α-SMA, Fn, and collagen, fixed cells were permeabilized with 0.05% Triton X-100 (VWR) in PBS (PBS-X), blocked in 1% BSA (Fischer Scientific) in PBS, and then incubated with primary antibodies directed against α-SMA (Abcam), Fn, and collagen (Millipore) overnight at 4°C. Subsequently, samples were labeled with species-specific AlexaFluor 488-conjugated secondary antibodies. The percentage of BrdU-positive cells was determined by manually counting five representative images for each sample for a total of three samples. Matrix thickness was determined by confocal analysis of Z-stack images (1-μm interval) captured with a Zeiss 710 confocal microscope. Differences inASC secretion of SDF-1 were evaluated via SDF-1 ELISA duo set (R&D) following 24 hours of incubation in serum-starved media and normalized to DNA content as measured from cell lysates by QuantiFluor dsDNA System (Promega) (n = 3/group). To assess the role of leptin deficiency in enhancing the profibrotic potential of *ob/ob* ASCs, cells were supplemented with 10 ng/ml leptin (R&D) for 5 days prior to analysis.

Western blot analysis

Tissue and cell lysates were prepared in RIPA buffer containing protease and phosphatase inhibitor cocktail (all from Thermo Scientific) as well as 1mM phenylmethylsulfonyl fluoride (Calbiochem). Protein concentrations were measured using a BCA kit (Thermo Scientific) and equal amounts of protein samples were loaded on gels (Bio-Rad), separated by reducing SDS-PAGE, and transferred to PVDF membranes (Bio-Rad). After blocking with 5% milk powder, membranes were incubated overnight (4°C) with primary antibodies raised against α-SMA, Fn, fibroblast activation

protein (FAP) (Millipore) and pFAK [397] (Invitrogen), as well as the house keeping proteins HSP90 (Santa Cruz), β-actin (Millipore), and GAPDH (Ambion). Following incubation with species-specific HRP-conjugated secondary antibodies (Novus Bio) chemiluminescence detection was performed using an ECL kit (Thermo Scientific). Densitometric analysis was performed with Image Lab (Biorad), Image J and Adobe Photoshop CS4.

Analysis of Fn conformation via FRET

Differences in Fn conformation were determined as described previously (*26, 55*). Briefly, $2x10^4$ ASCs from *ob/ob* and wild-type mice were seeded in Lab-Tek chamber slides (Thermo Scientific) pre-coated with 30 μg/ml unlabeled Fn (Invitrogen) in PBS (*n* = 3 samples/condition). Subsequently, human plasma Fn (only 8% FRET-labeled Fn with an excess of 92% unlabeled-Fn to prevent intermolecular energy transfer between adjacent proteins in fibers) was added to yield a final Fn concentration of 50 μg/ml necessary for FRET analysis. Twenty-four hours post-incubation, cells were fixed with 4% PFA, washed with PBS and then imaged using a Zeiss 710 confocal microscope with a 40x water immersion objective under conditions that prevented photobleaching. Z-stack images (1-μm interval) were captured at 6-8 randomly chosen areas following excitation with a 10% laser intensity through the 488 nm channel, and then the signals from both the donor (514-526 nm) and acceptor (566-578 nm) channels were collected. Image processing of the acceptor and donor images was performed as described previously (*55*). Briefly, MATLAB (MathWorks, Inc.) was used to compute the FRET intensity (ratio of acceptor and donor channels) of images, to calculate the mean and standard deviation of

the FRET intensities, and to compile FRET intensity data for histogram plotting. Then, Fn conformation was determined by pre-obtained calibration curves of FRET intensities as a function of chemically induced Fn denaturation as well as circular dichroism spectra of the denatured Fn, an indicator of Fn unfolding and β-sheet content, respectively (*26*).

Analysis of ECM stiffness via Surface Forces Apparatus

To measure the compressive elastic moduli of cell-free matrices deposited by *ob/ob* or wild-type ASCs, we used the Surface Forces Apparatus (SFA) (SurForce LLC) (*27*). For measurements, two mica surfaces (one holding the matrix) were mounted on a double cantilever of known spring constant (k = 980 N/m) and compressed with a bare mica surface from the top. The force acting between the surfaces was then measured as a function of surface separation (Fig. 3C). The two back-silvered, semicylindrical mica surfaces build an optical interferometer. For each pair, the bare (upper) surface used for indentation was kept in a desiccator until needed. The other (lower) surface was coated with 30 μg/ml of Fn (Invitrogen) in PBS, placed in a custom-made PDMS, and seeded with 2×10^4 wild-type or *ob/ob* ASCs. Following 24 hours of culture, matrices were decellularized (*56*).

To measure their compressive Young's modulus, paired discs were mounted in a crossed cylinder axis configuration, to obtain a well-defined flat circular junction equivalent to a sphere-on-flat like contact. The SFA chamber was filled with PBS at 37°C, keeping both discs fully immersed during the measurements. Individual samples were probed at four different positions approximately 0.5 mm apart. Each position was compressed at least 3 consecutive times with increasing normal force.

Compressive measurements were performed in the quasi-static regime, at the lowest speed achievable with our normal motor (V = 8 to 9 nm/s) to prevent any viscous contribution. The system was allowed to equilibrate for 20 minutes between each compressive cycle. Measured force-distance profiles were further analyzed to extract the compressive elastic moduli using the Johnson contact mechanics model (*57*), in which the indentation under compression (δ) between a sphere and a flat was related to normal force (*F*) by the following equation:

$$\frac{F}{R} = E\pi \frac{\delta^2}{D_0}$$

where *R* is the equivalent radius of curvature of the cylindrical discs (*R* ~ 2 cm), D_0 is the undistorted (prior to compression) thickness of the matrix, and *E* the compressive Young's modulus of the ECM (Fig. 3C).

Interstitial stiffness measurement by AFM

AFM nanoindentation measurements were performed on 4-μm thick, rehydrated paraffin sections of wild-type and *ob/ob* mammary tissues using a MFP-3D-AFM scanning probe microscope (Asylum Research) mounted onto an Olympus IX-71 inverted optical microscope. Interstitial regions were probed using a 5-μm diameter borosilicate glass sphere attached to a silicon nitride cantilever (Novascan Tech). The nominal spring constant *k* (~0.06 N/m) of the cantilever was determined by thermal calibration prior to each measurement. AFM measurements were performed in contact mode under quasi-static conditions (V = 20 nm/s) in PBS. For the analysis, full force-indentation loading curves were recorded over small indentations (approximately 20 nm in depth) and, since no adhesion was measured, were fitted to the Hertz spherical indentation model;

$$F = \frac{4}{3} E \sqrt{R} \delta^{\frac{3}{2}}$$

where F is applied force, R is the radius of the glass sphere ($R \sim 5$ μm), δ is indentation of tissue, and E is the Young's modulus of the tissue. Analysis was performed using IGOR PRO software (WaveMetrics). The Young's moduli (E) were calculated based on the resulting fit coefficients as the Poisson's ratio was set to 0.5. Four samples with 20-30 regions per sample were measured per condition ($n = 4$).

Analysis of ASC responses to obesity-mediated ECM changes

Decellularized matrices were used to study the impact of wild-type and *ob/ob* ECMs on ASC phenotype. Briefly, $3x10^4$ wild-type or *ob/ob* ASCs were seeded on Fn-coated Thermanox coverslips (Thermo Scientific) and cultured for 8 days after which cells were removed through detergent-based extraction as previously described (*56*). Absence of cellular residuals was confirmed using DAPI staining (not shown) and Western blot analysis of GAPDH (fig. S9). The decellularized matrices were blocked with 1% BSA at 4°C overnight prior to use. Subsequently, wild-type and *ob/ob* ASCs were cultured on the different decellularized ECMs in the presence and absence of Y-27632 (10 μg/ml) (Tocris) for 7 days. The number of α-SMA positive cells was assessed via IF image analysis as described above. Additionally, experiments were performed in which the matrices were pretreated with exogenous TGF-β (20 ng/ml) or anti-LAP (100 ng/ml) (both from R&D) at 37°C for an hour and washed twice with PBS prior to cell seeding. The quantity of matrix-bound TGF-β was measured by ELISA (R&D) of lysates from decellularized matrices.

Analysis of tumor cell responses to obesity-mediated ECM changes

To analyze ECM-induced variations in tumor cell behavior, MDA-MB231 and MCF10AT were cultured on the different decellularized matrices in low serum media (MDA-MB231: α-MEM, 1% FBS, 1% antibiotic; MCF10AT: DMEM/F12, 2% horse serum, 1% antibiotic) for 8 to 10 days (n = 3/condition). Cell growth was determined by counting trypsinized cells using a hemocytometer. Differences in FAK phosphorylation were determined by IF and Western blot analysis of pFAK[397], as described above. Tumor cell contractility was inhibited with Y27632 (10 μg/ml). To test potential effects of Fn conformational changes on MDA-MB231 growth, integrin engagement was inhibited with function-blocking αvβ3 (10 μg/ml) and/or α5β1 (10 μg/ml) integrin antibodies (Milllipore) prior to cell seeding and during the culture period. The role of wild-type and *ob/ob* ECMs in the disorganization of premalignant structures was determined by culturing MCF10AT acini on the different matrices in low serum media for 36 hours. To develop acini, MCF10AT (2,500 cells/well) were cultured in Lab-Tek chamber slides (Thermo Scientific) pre-coated with Matrigel (40 μl/well) (BD) for 10 days (*35*). Acini were isolated by multiple washes with ice-cold Tris-EDTA buffer (10 mM Tris buffer, 3 mM EDTA, and 0.2% BSA) and subsequent short-centrifugation at 120 g, as described (*35*). Acini disorganization was assessed by confocal microscopy following IF for β-catenin (Abcam), β4 integrin (Millipore), Fn, and nuclei. Acini surface area and height were analyzed by confocal image analysis of Z-stacks (2-μm intervals) using Image J (n = 100 acini/group) (Fig. 5B). For MCF10AT migration analysis, decellularized wild-type and *ob/ob* matrices were prepared in glass bottom dishes (MetTek). Matrices were fluorescently labeled by supplementing the respective ASC

cultures with Alexa Fluor 488-labeled Fn for 2 days prior to decellularization; MCF10AT, cells were labeled with the membrane dye Dil Vybrant Cell-Labeling Solutions (Molecular Probes, Inc.). Time lapse imaging was initiated 5 hours after seeding using an inverted Andor/Olympus IX-83 spinning disk confocal microscope (Olympus Corporation, Tokyo, Japan). Z-stack images were captured at 8 different locations per sample every 5 mins, for 5 hours. Cell motility was computed from the total distance of cell movement over time as measured with Image J.

Tumor cell migration studies

To investigate the effect of SDF-1 from *ob/ob* ASCs on tumor cell recruitment, a transwell migration assay was used. MDA-MB231 cells were seeded on collagen-coated transwell inserts (Corning Inc.), which were subsequently placed in wells that contained ASCs cultured in low serum media with or without SDF-1 antibody (50 μg/ml) (R&D). After 18 hours, transwell membranes were fixed with formalin, stained with DAPI, and imaged from the bottom to the top with a Zeiss 710 confocal microscope. Subsequently, the number of migrated MDA-MB231 cells was quantified via manual counting of DAPI- stained nuclei at the bottom of the membrane. To further confirm the importance of the SDF-1/CXCR4 signaling axis to varied MDA-MB231 migration, SDF-1 signaling was inhibited by blocking its corresponding receptor with a CXCR-4 antibody (25 μg/ml) (R&D) (n = 3/group).

Analysis of tumor-free human breast tissues

A previously published set of 29 tumor-free, human breast tissues categorized into normal, overweight and obese was used to assess the effect of obesity on interstitial fibrosis in humans (*37*). Specimens were collected from patients undergoing mastectomy whereby samples were harvested from either the contralateral breast or from quadrants not involved by the tumor to ensure that tumor-free tissue was analyzed. Paraffin sections were used for the analysis of collagen fiber structure by SHG imaging as well as levels of α-SMA positive cells. Furthermore, snap frozen tissue was used to analyze levels of TGF-β mRNA. Total RNA was isolated and processed as described previously (*37*). The forward and reverse primers for *TGF-β* were 5'-GAGCCTGAGGCCGACTACTA-3' and 5'-CGGAGCTCTGATGTGTTGAA-3'; and for *GAPDH* 5'-TTCTTTTGCGTCGCCAGCCGA-3' and 5'-GTGACCAGGCGCCCAATACGA-3'. Real-time PCR was conducted using 2x SYBR green PCR master mix on a 7500 HT real-time PCR system (Applied Biosystems), with expression determined using the $\Delta\Delta C_T$ analysis protocol. The quantity of crown-like structures in each breast sample (CLS-B) was determined as previously described and indicated as CLS-B index (*37*).

Analysis of patient-derived breast tumor specimens

Paraffin-embedded breast tumor specimens were obtained from existing archived samples of 17 lean and 18 obese breast cancer patients under the approval of IRB Study 0408007390 at Weill Cornell Medical College. Tumor specimens were categorized by the patient's body mass index (BMI = mass [kg]/(height [m])^2) whereby a BMI of < 25 and > 30 was considered lean and obese, respectively. The two cohorts were evenly matched for age, menopausal status, as well as subtype of breast cancer (table S1). In both groups,

the majority of patients (83%) had stage 3 breast cancer at diagnosis and the remainder (17%) had *de novo* stage IV breast cancer as their initial diagnosis. To assess the degree of desmoplasia, H&E-stained sections were scored by a pathologist in a blinded manner. Additionally, specimens were subjected to SHG image analysis of collagen as well as IF staining of α-SMA, Fn, and YAP/TAZ (clone sc101199; Santa Cruz) as described above. For the latter, images of 10 randomly selected areas of the whole tumor were captured per sample and subjected to image analysis; YAP/TAZ analysis was done on epithelial regions of the tumors as determined morphologically.

Gene ontology data analysis

To test the clinical link between obesity-mediated transcriptomic changes of ECM, cell adhesion, and inflammation, gene ontology analysis was performed based on previously published data of estrogen receptor (ER)+ breast cancer patients (*39*). A list of the most significantly differentially expressed genes across lean vs. obese patients was analyzed to identify enrichment for ECM-, adhesion-, and inflammation-related gene signatures. Pathway analysis was performed on the differentially expressed genes using the tool DAVID (*58*) to reveal enrichment for various known functional pathways. Favorable functional pathways were then selected based on significance ($P < 0.05$) and false- positive rate (Benjamini; FDR < 0.2). A co-expression analysis was performed using R statistical software to correlate the identified ECM-, inflammation-, and YAP/TAZ- related genes. Affymetrix gene expression values were evaluated to obtain expression- based correlations, and significantly co-expressed genes ($P < 0.05$) were selected based on adjusted P value (FDR < 0.2).

Supplementary Figures

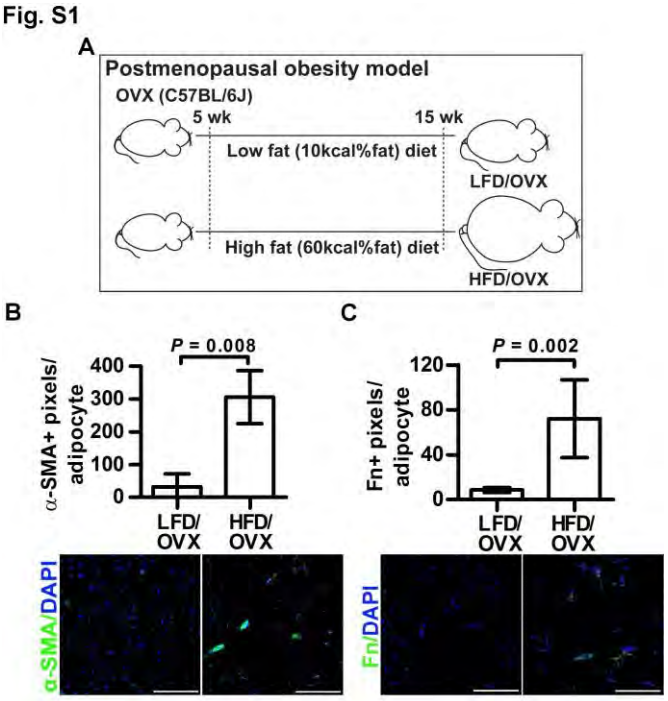

Fig. S1: Obesity promotes interstitial fibrosis in breast adipose tissue after menopause. (**A**) Ovariectomized (OVX) mice subjected to a high-fat diet (HFD) for 10 weeks were used as a postmenopausal obesity model; age-matched OVX mice fed a low-fat diet (LFD) served as controls. (**B** and **C**) IF analysis of α-SMA (B) and fibronectin (Fn) (C) content in mammary fat from OVX mice. Scale bars, 200 μm. Data are means ± SD (*n* = 5 to 6/group). *P* values determined by unpaired Student's two-tailed t-tests.

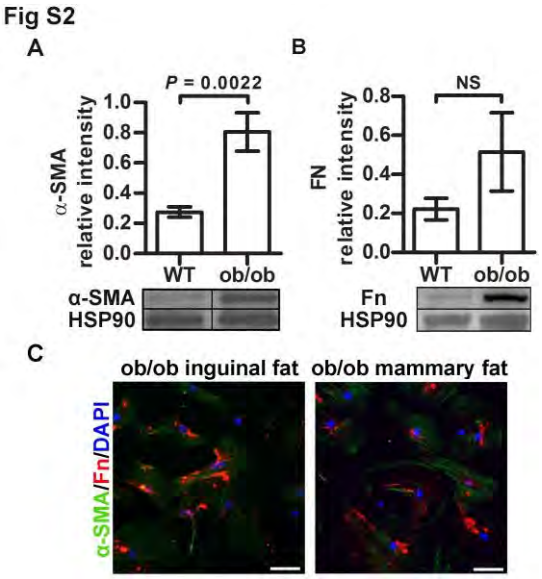

Fig. S2. Inguinal depots of adipose tissue feature markers of interstitial fibrosis (**A, B**) Western blot analysis of α-SMA (A) and fibronectin (Fn) (B) levels in inguinal adipose tissue (a mix of s.c. and mammary fat) from *ob/ob* or wild-type (WT) mice. Data indicate average α-SMA or Fn intensity relative to HSP90 intensity with ± SD (n = 3/condition). P values were determined by unpaired two-tailed t-tests. NS, not significant.
(**C**) IF analysis of α-SMA and Fn levels of *ob/ob* ASCs from inguinal and mammary fat. Scale bars, 100 μm.

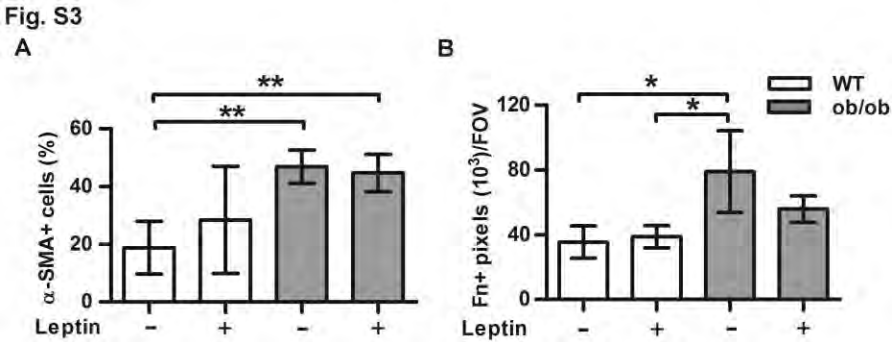

Fig. S3: The profibrotic potential of *ob/ob* ASCs is not due to leptin deficiency. (**A** and **B**) IF analysis of α-SMA expression (A) and fibronectin (Fn) levels (B) of ASCs with and without leptin supplementation. Data are means ± SD (n = 3/group). *$P < 0.05$, **$P < 0.01$, by two-way analysis of variance (ANOVA).

Fig. S4

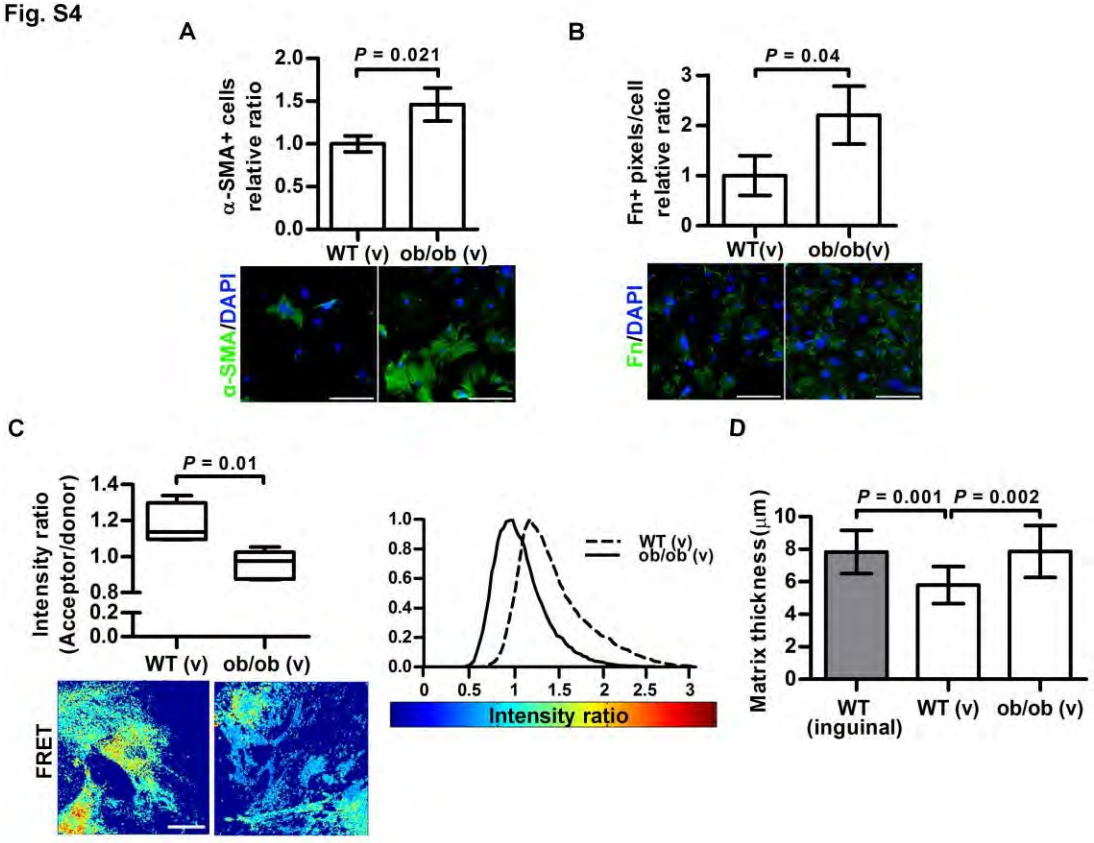

Fig. S4: Obesity-associated ASCs promote fibrotic ECM remodeling in visceral fat. (**A** and **B**) IF analysis of α-SMA (A) and fibronectin (Fn) (B) of ASCs isolated from visceral fat. Data are means ± SD (n = 3/condition). (**C**) FRET analysis of Fn conformation in the matrices deposited by ASCs from visceral depots. (Left) Pseudocolored Fn matrices; box and whiskers plots of FRET intensity of 6-8 representative fields of view per condition. (Right) Histograms of the corresponding distributions of FRET intensity (n = 4-5/condition). P values in (A to C) were determined by unpaired two-tailed t-tests. (**D**) Confocal analysis of matrix thickness. Data are means ± SD (n = 10-15/condition). P values were determined by one-way ANOVA. All scale bars, 200 μm.

Fig. S5

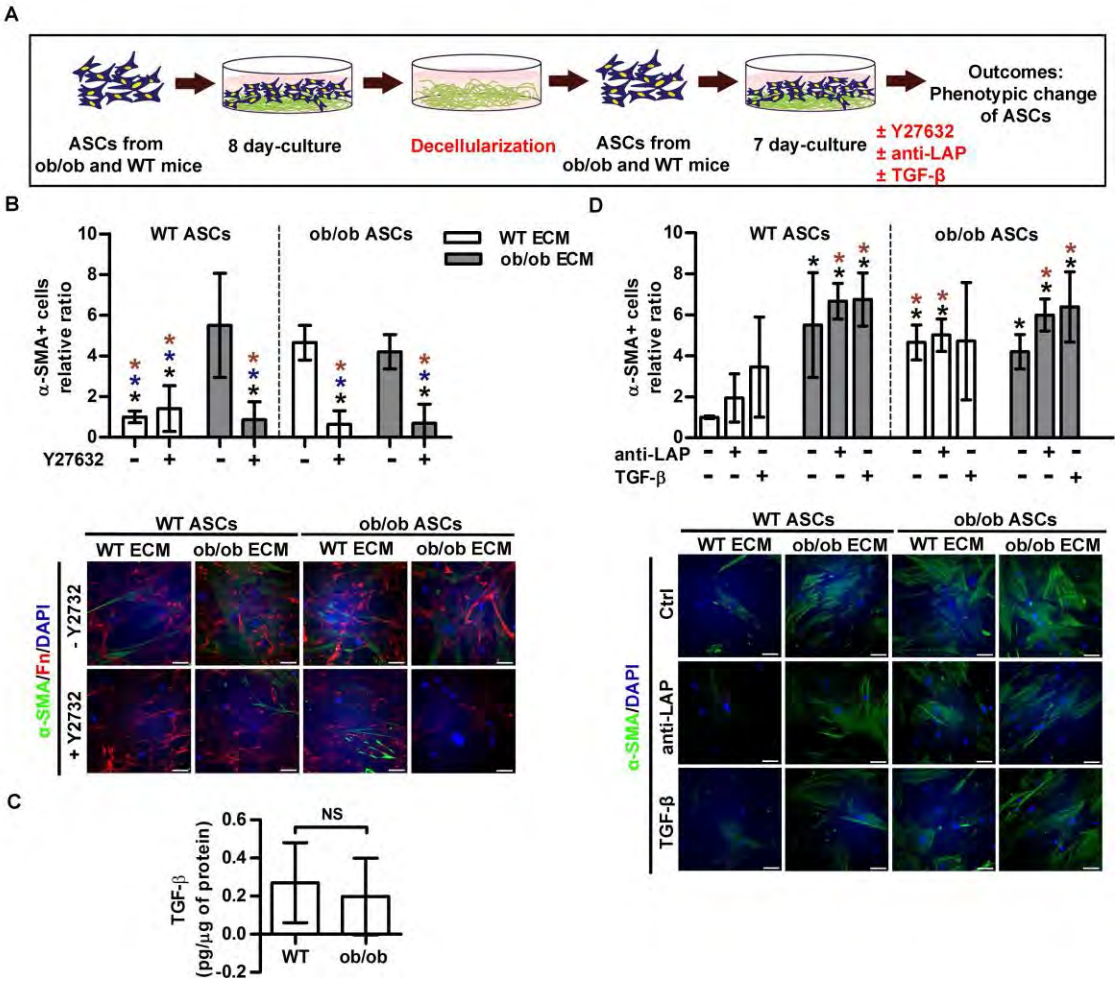

Fig. S5: ECMs deposited by obesity-associated ASCs promote myofibroblast differentiation (**A**) Schematic illustrates that matrices deposited by WT and *ob*/*ob* ASCs (WT and *ob*/*ob* ECM, respectively) were decellularized and reseeded with either WT or *ob*/*ob* ASCs to examine their effect on ASC myofibroblast differentiation. (**B**) IF analysis of α-SMA levels in WT and *ob*/*ob* ASCs cultured on *ob*/*ob* or WT ECMs, in the presence or absence of Y27632. Scale bars, 50 μm. (black asterisk) **P* < 0.05 versus WT-ASCs cultured on *ob*/*ob* ECM; (blue asterisk) **P* < 0.05 versus *ob*/*ob* ASCs cultured on WT ECM; (red asterisk) **P* < 0.05 versus *ob*/*ob* ASCs cultured on *ob*/*ob* ECM; two-way ANOVA. (**C**) ELISA of matrix-bound TGF-β in lysates prepared from decellularized WT and *ob*/*ob* matrices. NS, not significant, by unpaired two-tailed t-test. (**D**) The impact of TGF-β on phenotypic changes of ASCs was analyzed by saturating decellularized matrices with exogenous TGF-β prior to cell seeding and by blocking TGF-β activation using a LAP antibody. Scale bars, 50 μm. (black asterisk) **P* < 0.05 versus WT-ASCs cultured on WT ECM; (red asterisk) **P* < 0.05 versus WT-ASCs cultured on WT ECM with a LAP antibody; two-way ANOVA. Data in (B to D) are means ± SD (*n* = 3/condition).

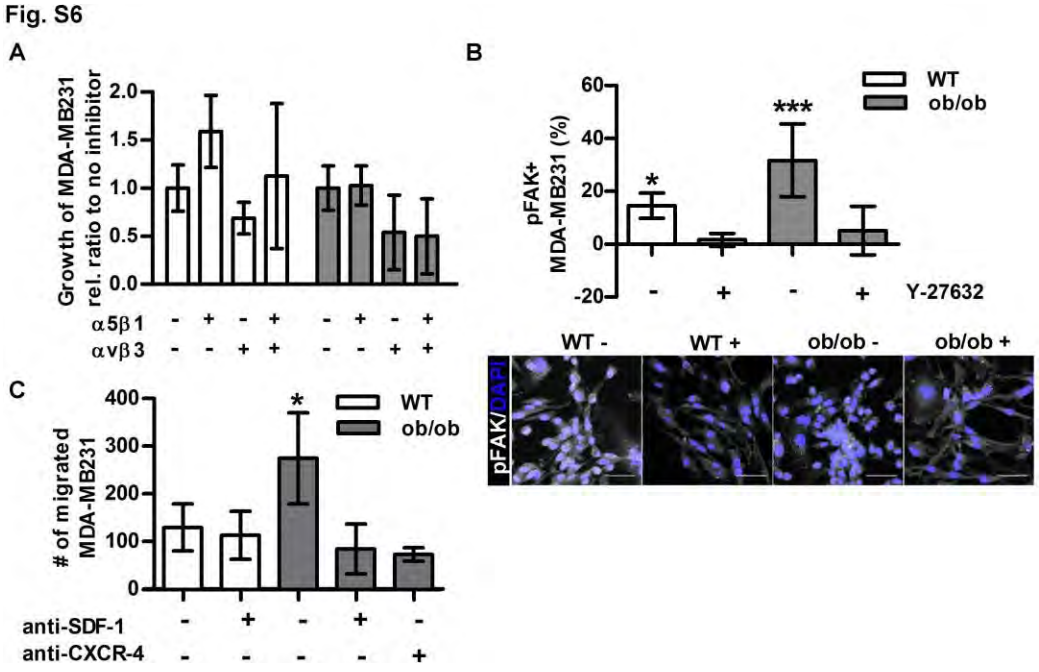

Fig. S6: Physicochemical cues of *ob*/*ob* ECMs modulate MDA-MB231 behavior. (**A**) Analysis of MDA-MB231 growth on WT and *ob*/*ob* ECMs in the presence and absence of α5β1 and αvβ3 function-blocking antibodies. (**B**) IF analysis of pFAK levels in MDA-MB231 cultured on the different decellularized ECMs in the presence and absence of Y27632. **P* < 0.05 versus WT with Y27632, ****P* < 0.001 versus all other groups. Scale bars, 50 μm. (**C**) Transwell migration assays of MDA-MB231 in response to SDF-1 secreted by *ob*/*ob* or WT ASCs. SDF-1–dependent migration of MDA-MB231 cells was assessed by antibody-based inhibition of both ASC-secreted SDF-1 and the tumor cells' cognate CXCR4 receptor. **P* < 0.05 versus all other groups. In (A to C), data are means ± SD (*n* = 3/condition), and *P* values were determined by two-way ANOVA.

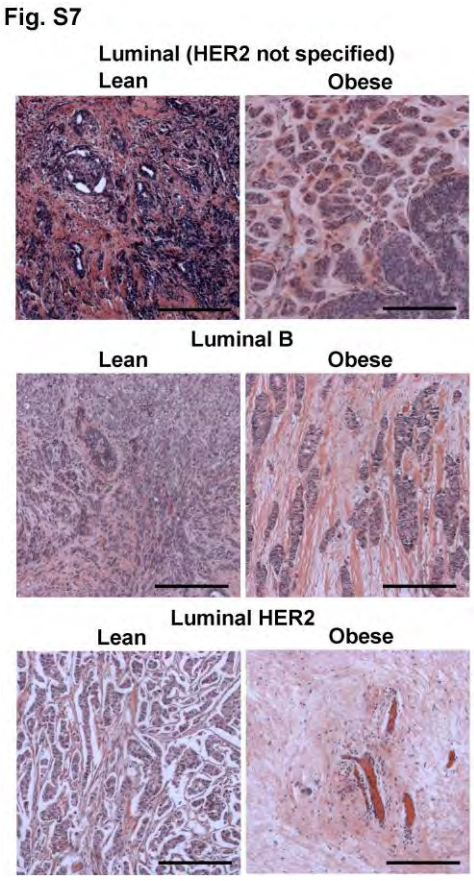

Fig. S7: H&E images of breast tumors with different subtypes. Representative H&E images of different tumor subtypes used in this study. Luminal A tumors are shown in Fig. 7A. All scale bars, 200 μm.

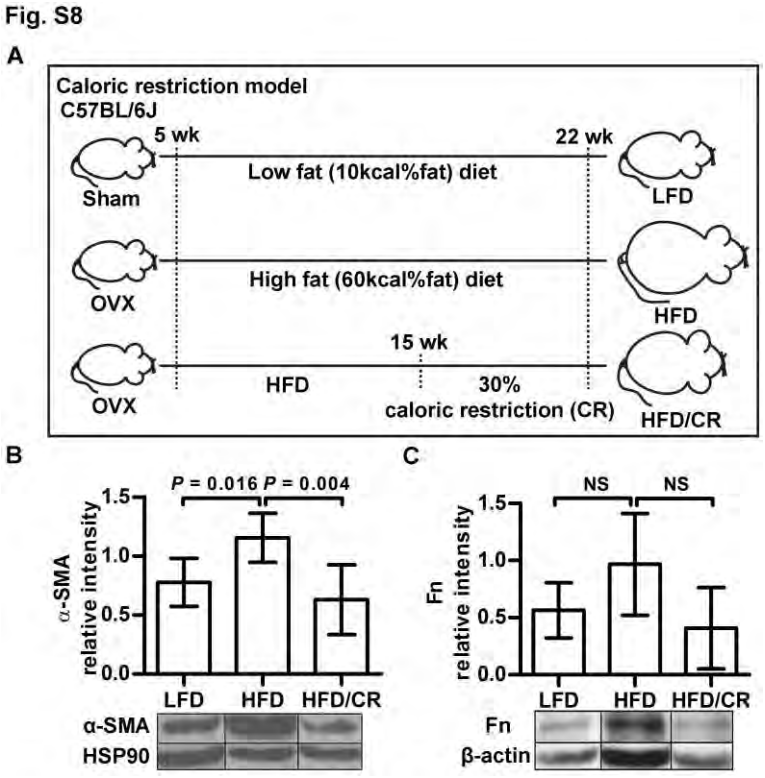

Fig. S8: Caloric restriction decreases fibrosis in mammary fat of obese mice. (**A**) Schematic showing the experimental design for caloric restriction experiments: ovariectomized mice (OVX) were fed with HFD for 10 weeks with and without 30% of caloric restriction for 7 weeks. (**B** and **C**) Western blot analysis of α-SMA (B) and fibronectin (Fn) (C) content in excised mammary fat from mice on LFD or HFD with or without caloric restriction (CR). Data are means ± SD (n = 5 to 6/group). P values were determined by one-way ANOVA. NS, not significant.

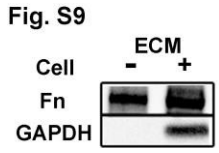

Fig. S9: Decellularized ECMs do not contain cellular residuals. GAPDH WB analysis of lysates prepared from *ob/ob* ASC cultures prior to (Cell +) and following (Cell -) decellularization to confirm that decellularized matrices did not contain cell-associated residuals.

Table S1: Subtypes, demographics, and desmoplastic grade of lean and obese breast cancer samples. Statistical examination of clinical specimens from 17 lean and 18 obese breast cancer patients to confirm parity of age, cancer subtype, and menopausal status between the two cohorts. Histopathological analysis was performed to determine the desmoplastic grade of the tumor specimens. Grades 1, 2 and 3 indicate mild, moderate, and severe desmoplasia, respectively. *P* values were determined by Fisher's exact test.

Cancer subtype	Classification criteria
Luminal (HER2 status not specified)	ER+ and/or PR+, and HER2+/−
Luminal A	ER+ and/or PR+, HER2−, and low Ki67 (<14%)
Luminal B	ER+ and/or PR+, HER2−, and high Ki67 (>14%)
Luminal A/B	ER+ and/or PR+, HER2−, and no Ki67 available
Luminal HER2	ER+ and/or PR+, and HER2+
HER2/neu enriched	ER−, PR−, and HER2+
Triple negative	ER−, PR−, and HER2−
Basal-like	ER−, PR−, HER2−, and CK5/6 and/or EGFR+

Variable		Body type		*P*- value
		Lean (*n* = 17)	Obese (*n* = 18)	
Age	< 30	1	0	1
	30 ≤ age < 40	6	6	
	40 ≤ age < 50	3	3	
	50 ≤ age	7	9	
	Median age	43	43	
Cancer type	Luminal (HER2 status not specified)	4 (23.5%)	4 (22.2%)	0.782
	Luminal A	1 (5.9%)	3 (16.7%)	
	Luminal B	3 (17.7%	2 (11.1%)	
	Luminal A/B	4 (23.5%)	2 (11.1%)	
	Luminal HER2	2 (11.8%)	3 (16.7%)	
	HER2/neu enriched	1 (5.9%)	0	
	HER2 negative	0	1 (5.6%)	
	ER/PR negative	1 (5.9%)	0	
	Triple negative	1 (5.9%)	1 (5.6%)	

	Basal-like	0	2 (11.1%)	
Menopausal status	Pre-menopausal	10 (58.8%)	10 (55.6%)	1
	Post-menopausal	7 (41.2%)	8 (44.4%)	
Desmoplastic grade	Grade 1	6 (35.3%)	0	0.006
	Grade 2	9 (52.9%)	8 (44.4%)	
	Grade 3	2 (11.8%)	10 (55.6%)	

Table S2. Gene ontology data analysis. Bioinformatics analysis of published data to test whether obesity enriches functional pathways associated with ECM-, adhesion-, and inflammation-related gene signatures in estrogen receptor–positive breast cancer patients.

Category	Term	*P*-value	Benjamini (FDR)
ECM related gene sets			
SP_PIR_KEYWORDS	Secreted	2.67E-15	7.30E-13
SP_PIR_KEYWORDS	Signal	6.84E-13	9.38E-11
UP_SEQ_FEATURE	Signal peptide	8.76E-13	4.46E-10
GOTERM_CC_FAT	GO:0005576~extracellular region	9.75E-12	1.76E-09
GOTERM_CC_FAT	GO:0044421~extracellular region part	4.96E-11	4.47E-09
GOTERM_CC_FAT	GO:0005615~extracellular space	6.06E-11	3.64E-09
UP_SEQ_FEATURE	Disulfide bond	6.49E-09	1.65E-06
SP_PIR_KEYWORDS	Disulfide bond	1.55E-08	1.42E-06
SP_PIR_KEYWORDS	Glycoprotein	6.21E-07	4.26E-05
Cell adhesion related gene sets			
SP_PIR_KEYWORDS	Cell adhesion	0.009	0.097
Inflammation related gene sets			
GOTERM_BP_ALL	GO:0050727~regulation of inflammatory response	0.002	0.055
GOTERM_BP_FAT	GO:0050727~regulation of inflammatory response	0.002	0.109
GOTERM_BP_ALL	GO:0006954~inflammatory response	0.007	0.132

Table S3: Correlation of YAP/TAZ-regulated genes with obesity-dependent ECM remodeling/inflammation. Bioinformatics analysis of published data from obese ER+ breast cancer patients (*39*) to test whether some of the eight obesity- induced genes that are common to both ECM- and inflammation-related pathways correlate with the YAP/TAZ-regulated genes *CTGF* and *ANKRD1*.

Inflammation -ECM gene probe ID	NCBI gene name	Description	Correlation	*P*-value	Adjusted *P*-value (FDR)
YAP/TAZ related gene *ANKRD1*					
202859_x_at	IL8	Interleukin 8	0.18	7.45E-06	1.79E-05
203400_s_at	TF	Transferrin	0.16	2.58E-05	5.15E-05
205382_s_	CFD	Complement factor D (adipsin)	-0.08	0.043	0.057
207175_at	ADIPOQ	Adiponectin, C1Q and collagen domain containing	0.11	0.007	0.011
207400_at	NPY5R	Neuropeptide Y receptor Y5	0.35	0	0
211506_s_at	IL8	Interleukin 8	0.12	0.002	0.004
211652_s_at	LBP	Lipopolysaccharide binding protein	0.36	0	0
214063_s_at	TF	Transferrin	0.22	3.02E-08	1.21E-07
214461_at	LBP	Lipopolysaccharide binding protein	0.19	2.77E-06	8.32E-06
YAP/TAZ related gene *CTGF*					
203400_s_at	TF	Transferrin	0.086	0.032	0.13
207175_at	ADIPOQ	Adiponectin, C1Q and collagen domain containing	0.088	0.028	0.13
203400_s_at	TF	Transferrin	0.12	0.003	0.035